

Mineralogy and elasticity of the oceanic upper mantle: Origin of the low-velocity zone

Lars Stixrude and Carolina Lithgow-Bertelloni

Department of Geological Sciences, University of Michigan, Ann Arbor, Michigan, USA

Received 5 January 2004; revised 7 December 2004; accepted 20 December 2004; published 15 March 2005.

[1] We use a new method to construct an upper mantle model based on self-consistent computation of phase equilibria and physical properties. Computation of the isotropic elastic wave velocities of a pyrolytic bulk composition in thermodynamic equilibrium shows a distinct low-velocity zone with a minimum velocity $V_S = 4.47 \text{ km s}^{-1}$ along the 100 Ma geotherm. In the vicinity of the low-velocity zone the velocity of this null hypothesis is approximated along oceanic geotherms by $V_S = 4.77 + 0.0380(P, z/29.80) - 0.000378(T - 300)$, with pressure P in GPa, depth z in km, temperature T in K, and velocity V_S in km s^{-1} . The null hypothesis predicts a minimum V_S 0.1–0.2 km s^{-1} higher than that in seismological models of 100 Ma Pacific. We find that dispersion, estimated solely on the basis of seismological attenuation models, can account for this residual velocity deficit. Except in the immediate vicinity of the ridge ($t < 5 \text{ Ma}$), a solid-state low-velocity zone provides a satisfactory quantitative explanation of seismic observations. We do not find a satisfactory explanation for the magnitude of the Gutenberg discontinuity or for the high shear wave velocity gradient zone.

Citation: Stixrude, L., and C. Lithgow-Bertelloni (2005), Mineralogy and elasticity of the oceanic upper mantle: Origin of the low-velocity zone, *J. Geophys. Res.*, 110, B03204, doi:10.1029/2004JB002965.

1. Introduction

[2] The low-velocity zone was first recognized by Gutenberg [1959] and has been a persistent feature of global seismological models and of local models in oceanic and tectonically active regions [Anderson, 1989]. By virtue of its intermediate position between the upper thermal boundary layer and the nearly adiabatic interior, the low-velocity zone may hold important clues to the relationship of the Earth's internal dynamics to plate tectonics and the origin of the crust. The low-velocity zone nearly coincides in depth with the region of the mantle identified as the asthenosphere, a region of lowered viscosity that may be an essential enabler of plate motions [Richards *et al.*, 2001]. Electrical conductivity measurements also show anomalous values in a depth range that is similar to that of the low velocity zone and the asthenosphere [Shankland and Waff, 1977].

[3] The low-velocity zone is characterized by negative velocity gradients: velocity decreasing with increasing depth. The sign of the velocity gradient is not remarkable in itself. Negative velocity gradients will appear whenever the thermal gradient exceeds a critical value such that the increase of velocity with compression is overcome by the decrease of velocity on heating. For olivine and other mantle minerals, the critical gradient for shear waves is modest (few kelvins per kilometer), so that one expects negative velocity gradients to be widespread in the shallow upper mantle on the basis of heat flow observations [Anderson *et al.*, 1968; Birch, 1969]. The origin of the low-velocity zone then is a

quantitative issue that demands an analysis of the magnitude of the negative velocity gradients and the absolute value of velocity in the low-velocity zone, and is best discovered by comparing the velocity to that of a null hypothesis that nearly characterizes seismic wave propagation throughout the rest of the mantle.

[4] Most previous investigations of the origin of the low-velocity zone have been based on comparison of the observed velocity to the calculated elastic wave velocity of an isotropic, subsolidus, equilibrium assemblage of constant bulk composition. These previous studies had important limitations, particularly in the definition and quantification of the null hypothesis. Some studies assumed a pure olivine composition [Birch, 1969; Schubert *et al.*, 1976; Karato and Jung, 1998], which accounts for no more than 60% of the upper mantle. Phase equilibria in the nonolivine fraction are important because the relative proportions of pyroxene and garnet change significantly over the relevant pressure range and because these two minerals have very different velocities. Previous studies have also been limited by the experimental data available at the time. One was completed before any data on pressure derivatives were available [Birch 1969], while others [Green and Liebermann, 1976; Schubert *et al.*, 1976; Karato and Jung, 1998] adopted values of pressure and/or temperature derivatives that violate recent experimental data taken over a range of pressure that encompasses the low-velocity zone. The study of Sato *et al.* [1989] was also based on data collected at pressures lower than are typical of the low-velocity zone.

[5] The limitations of previous studies lead us to reexamine the widely held notion that properties atypical of the mantle are required to explain the low-velocity zone,

such as the presence of partial melt [Lambert and Wyllie, 1968; Anderson and Sammis, 1969; Ringwood, 1969; Birch, 1969; Green and Liebermann, 1976; Sato *et al.*, 1989] or locally enhanced influence of bound water [Karato and Jung, 1998]. In particular, we seek to reexamine the null hypothesis and investigate whether the low-velocity zone may have a solid state origin. Desirable properties of the null hypothesis are that it be experimentally and theoretically well defined, and depend on a minimum number of variables. The null hypothesis that we adopt, and which satisfies these criteria is defined by (1) seismic wave propagation in the elastic limit (i.e., no dispersion), (2) isotropy, that is a randomly oriented polycrystalline aggregate, (3) absence of partial melt, (4) homogeneous bulk composition, and (5) thermodynamic equilibrium. This combination of criteria is powerful because the calculated velocity depends, within the uncertainty of experimental measurements and the intrinsic uncertainty of Voigt and Reuss bounds, only on the specification of pressure, temperature, and major element composition. Furthermore, we may explore quantitatively the possible effects of a number of other variables that may be relevant, but which are less well constrained both as to their prevalence in the mantle, and their influence on the velocity. These variables include kinetics, grain size, dislocation density, dislocation motion, dynamic recrystallization, amount and geometry of partial melt, and minor and trace element composition.

[6] Our calculations take full advantage of the vast increase in knowledge of the acoustic velocities of upper mantle minerals by incorporating the most recent experimental data. Unlike some previous analyses, we also consider the phase equilibria of the upper mantle; this means that we are able to account for the nonolivine fraction and phase transformations in this fraction over the pressure range of the low-velocity zone. We present a new and general method that provides a unified description of the elasticity and phase equilibria of multicomponent, multiphase assemblages, and which allows us to construct Earth models that specify the variation of mineralogy and seismic wave velocities with pressure and temperature, and which are directly comparable to seismological observations.

[7] We focus primarily on the oceanic low-velocity zone, although we also show results along a typical continental geotherm for comparison. The following sections outline our method of self-consistent determination of phase equilibria and physical properties (section 2), results (section 3) and comparison with seismological observations (section 4). Comparison of the null hypothesis with seismological models reveals similarities, particularly in the presence of a prominent low-velocity zone, but important differences as well, including the magnitude of the lowest velocities, the Gutenberg discontinuity, and the magnitude of the velocity gradient beneath the low-velocity zone. These differences lead us to consider other factors that may be relevant in section 5, including heterogeneous major element composition, partial melt, and dispersion.

2. Methods

[8] Quantification of the null hypothesis postulated in the introduction can be reduced to the following problem: given an isolated, homogeneous system of fixed bulk composi-

tion, \mathbf{x} in thermodynamic equilibrium at pressure P and temperature T , determine the elastic wave velocities. The problem can be divided into three steps: (1) Find the equilibrium phase assemblage: the phases that are stable, their relative proportions and their compositions in equilibrium. (2) Determine the seismic wave velocities of the individual phases at their equilibrium compositions for the \mathbf{x} , P , and T of interest in the elastic limit. (3) Determine the seismic wave velocity of the aggregate in the elastic limit, for which we adopt the Voigt-Reuss-Hill theory [Watt *et al.*, 1976].

[9] To our knowledge, the first two aspects of the problem: an accurate account of geophysically relevant physical properties and phase equilibria, have not been treated self-consistently before. There have been many previous syntheses of portions of mantle thermodynamics, but many of these models are incomplete, because critical aspects of mantle physics cannot be derived from them. Such studies can be divided into two classes on the basis of their primary motivations: (1) to understand phase equilibria [Berman, 1988; Holland and Powell, 1990; Fei and Saxena, 1990; Ghiorso and Sack, 1995] and (2) to understand physical properties [Weidner, 1985; Duffy and Anderson, 1989]. Those focused on phase equilibria typically do not include an account of elastic constants other than the bulk modulus, while those focused on physical properties, including descriptions of the equation of state, or the elastic moduli, typically do not permit computation of phase equilibria.

[10] More recently there has been increasing interest in the development of models that attempt an accurate description of both phase equilibria and physical properties. In the construction of such models, adherence to thermodynamic self-consistency is important because it allows one to take maximum advantage of the multiple internal redundancy of different types of experimental measurements, thereby optimizing the robustness and scope of the model. Thermodynamic self-consistency is embodied in the Maxwell relations, equalities between apparently unrelated quantities such as thermal expansivity and the pressure dependence of the entropy, that provide important cross checks. In addition to satisfying the Maxwell relations, a thermodynamic model should also treat physical properties and phase equilibria self-consistently, a relationship exemplified by the Classius-Clapeyron equation. Self-consistency insures, for example, that the pressure-temperature slope of phase boundaries are consistent with the density and entropy of the phases involved. What might be termed hybrid models are thus not self-consistent: A model of physical properties is supplemented with an account of phase equilibria from an independent source such as a tabular or graphical summary of experimental data [Ita and Stixrude, 1992; Vacher *et al.*, 1998; Cammarano *et al.*, 2003; Hacker *et al.*, 2003]. Other models have supplemented phase equilibrium calculations with higher-order derivatives of physical properties that may violate Maxwell relations by not properly relating, for example, the temperature dependence of the bulk modulus to the pressure dependence of the thermal expansivity [Sobolev and Babeyko, 1994].

[11] Our approach, which we have emphasized in our previous work [Stixrude and Bukowski, 1990; Ita and Stixrude, 1992; Stixrude and Bukowski, 1993], is based on

Table 1. Bulk Compositions^a

Component	Pyrolite ^b	Harzburgite ^c	Pyroxenite ^d
SiO ₂	38.66	36.04	41.75
MgO	48.53	57.14	22.42
FeO	5.72	5.41	6.00
CaO	3.50	0.44	13.59
AlO _{3/2}	3.59	0.96	16.24

^aIn mol %.^bRingwood [1979].^cIrfune and Ringwood [1987].^dHirschmann *et al.* [2003].

the concept of fundamental thermodynamic relations, or potentials, the derivatives and Legendre transformations of which yield self-consistently all phase equilibria and physical properties from a single functional form. Extensions of our previous work to an arbitrary number of components and to shear elasticity are outlined in sections 2.1 and 2.2, respectively. In this study, we will focus on the ranges of pressure and temperature that are relevant for the upper mantle and on a simplified five-component model: CaO, FeO, MgO, Al₂O₃, SiO₂ (CFMAS) of the bulk composition of this region (Table 1). Our method is general and can be applied to larger numbers of chemical components as experimental data on more complex chemical compositions (e.g., Na₂O, H₂O, etc.) continue to be collected, and to conditions of higher pressure and/or temperature. The new method is discussed in more detail in a forthcoming publication [Stixrude and Lithgow-Bertelloni, 2005].

2.1. Phase Equilibria

[12] In order to determine the equilibrium phase assemblage, we minimize the total Gibbs free energy G of the aggregate with respect to the amounts of all species (end-members or phase components) of all phases, at constant pressure P , and temperature T , subject to the constraint of constant bulk composition

$$G(\mathbf{n}) = \sum_{i=1}^{\text{species}} n_i (\mu_{0i} + RT \ln a_i) \quad (1)$$

where \mathbf{n} is a vector containing the amounts of the species, μ_{0i} is the Gibbs free energy of the pure species, a_i is its activity in solution, and R is the gas constant. The problem is nonlinear (logarithmic term in the activity), multidimensional, and unstable for trace amounts of species (again the logarithmic term). We adopt the method of Harvie *et al.* [1987] whereby species and phases may be explicitly removed from the minimization (their amounts set explicitly to zero). The stability and speed of solution is dramatically improved by reducing the number of variables to the set of vectors that span the null space of the linear problem

$$A_{ij}n_j = b_i \quad (2)$$

where A_{ij} , the stoichiometric coefficient matrix, has dimensions $s \times c$ where s is the number of species, c is the number of components, and b_i is a vector of length c containing the amounts of the components. Physically, the vectors that span the null space (dimensionality $s - c$) represent the reactions that leave the bulk composition invariant. These reaction directions are efficiently identified

via QR decomposition of the nonsquare matrix A_{ij} . With this setup of the problem, the actual multidimensional minimization is performed with comparable efficiency by conjugate gradient, quasi-Newton, or simulated annealing methods [Press *et al.*, 1992].

2.2. Physical Properties

[13] The properties of pure species (end-members) including the μ_{0i} in equation (1) are specified by the fundamental thermodynamic relation, $F(e_{ij}, V, T)$ where F is the Helmholtz free energy, V is volume, and e_{ij} is the strain tensor that specifies infinitesimal deformation about the prestressed state, which is assumed to be hydrostatic. For the isotropic portion $F(V, T)$, we follow our previous work and use the integrated form of the Mie-Grüneisen relation with the Birch-Murnaghan equation of state for the ‘cold’ part, and the quasi-harmonic Debye-Grüneisen approximation for the thermal part [Stixrude and Bukowinski, 1990]. Phase equilibria, and all isotropic physical properties (bulk modulus, density, heat capacity, etc.) are specified by the following seven parameters: Helmholtz free energy F_0 , volume V_0 , bulk modulus K_0 , pressure derivative of bulk modulus K'_0 , Debye temperature θ_0 , Grüneisen parameter γ_0 , and q_0 (logarithmic volume derivative of γ) at the reference state ($P_0 = 0$, $T_0 = 300$ K). Values of these parameters for the relevant species are updated from Ita and Stixrude [1992]. The activities of species are specified by symmetric regular solution or ideal models [Stixrude and Bukowinski, 1993]. A more detailed discussion of the choice of phases, species, and values of parameters is given in Appendix A.

[14] By forming the appropriate derivatives of the Helmholtz free energy with respect to strain [Davies, 1974] one finds for the adiabatic elastic constants

$$c_{ijkl}(V, T) = (1 + 2f)^{5/2} \left[c_{ijkl0} + (3K_0 c'_{ijkl0} - 5c_{ijkl0})f + \dots \right] + \left(\frac{\gamma_{ij}\delta_{kl} + \gamma_{kl}\delta_{ij}}{2} + \gamma_{ij}\gamma_{kl} - \eta_{ijkl} \right) \frac{\Delta E_{\text{TH}}(V, T)}{V} \quad (3)$$

where subscript 0 refers to the reference state ($P = 0$, $T_0 = 300$ K), primes indicate pressure derivatives, $f = [(V_0/V)^{2/3} - 1]/2$ is the Eulerian finite strain, K is the bulk modulus, E is the internal energy, ΔE_{TH} is the difference in thermal energy between T and T_0 , γ_{ij} is the appropriate tensorial generalization of the Grüneisen parameter [Davies, 1974], and η_{ijkl} is the tensorial generalization of γq

$$\eta_{ijkl} = \left(\frac{\partial \gamma_{ij}}{\partial e_{ij}} \right)_T \quad (4)$$

The first term in (equation (3)) describes the dependence of the elastic constants on compression at the reference temperature and is equivalent to that derived by Davies [1974]. The second term is the thermal contribution and reduces to the appropriate Debye-Grüneisen result in the special case of the bulk modulus [Ita and Stixrude, 1992].

[15] We are interested here in the shear modulus and bulk modulus. For the shear modulus of an isotropic material (equation (3)) reduces to

$$G(V, T) = (1 + 2f)^{5/2} \left[G_0 + (3K_0 G'_0 - 5G_0)f + \dots \right] - \eta_s \frac{\Delta E_{\text{TH}}(V, T)}{V} \quad (5)$$

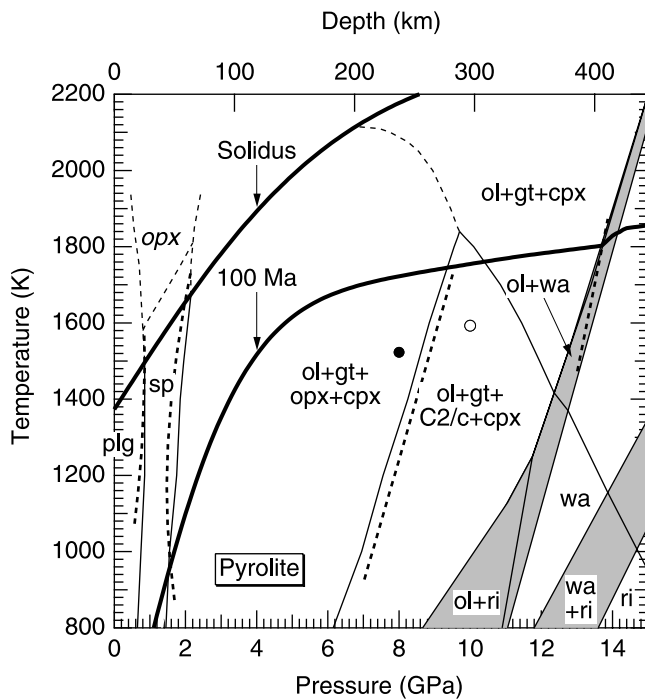


Figure 1. Phase diagram of pyrolite in the upper mantle. Superimposed on our computed phase diagram (light solid lines and shading) are our computed geotherm for 100 Ma oceanic lithosphere and the dry solidus (bold solid lines) taken from *McKenzie and Bickle* [1988] and *Zhang and Herzberg* [1994]. In light dashed lines we show our computed fictive supersolidus extension of the spinel phase boundaries to illustrate the proximity of mantle compositions to the spinel-out transition and the high-temperature portion of the opx-out transition, which is not realistic. Subsolidus experimental data are shown in bold dashed lines for plagioclase to spinel- to garnet-facies transitions in the CMAS system [*Wood and Holloway*, 1984], orthopyroxene to C2/c transition in MgSiO_3 [*Pacalo and Gasparik*, 1990], and olivine to wadsleyite transition in the olivine system for $\text{Fe}/(\text{Fe} + \text{Mg}) = 0.1$ [*Katsura and Ito*, 1989]. Solid circle represents the highest-pressure observation of orthopyroxene, and open circle represents lowest-pressure observation free of orthopyroxene [*Irfune and Isshiki*, 1998]. Abbreviations for all phases are defined in Table A1.

where we have assumed that the tensor η_{ijkl} is isotropic and have identified its shear- and volume-sensitive parts η_S and η_V , respectively, as

$$\eta_{ijkl} = \eta_V \delta_{ij} \delta_{kl} + \eta_S \left(\delta_{ik} \delta_{jl} + \delta_{il} \delta_{jk} - \frac{2}{3} \delta_{ij} \delta_{kl} \right) \quad (6)$$

with $\eta_V = q\gamma$, where δ_{ij} is the Kroenecker delta. The first term in equation (5) is identical to that of *Davies and Dziewonski* [1975] [see also *Sammis et al.*, 1970]. At this level of theory, specification of the shear modulus as a function of pressure (volume) and temperature requires three parameters in addition to those that define the isotropic portion of the fundamental relation: the shear modulus (G_0), its pressure derivative (G'_0), and the value of η_S at ambient conditions (η_{S0}). We assume that the ratio

η_S/V is independent of volume, i.e., $\eta_S = \eta_{S0}(V/V_0)$. Although we focus here on the isotropic average of η_{ijkl} , our formulation is general and capable of describing anisotropic properties.

3. Results

3.1. Phase Diagram

[16] Seven phases are stable in the upper mantle exclusive of the transition zone in the system under consideration: anorthite (plg), spinel (sp), olivine (ol), orthopyroxene (opx), clinopyroxene (cpx), the high-pressure polymorph of Mg-rich orthopyroxene of C2/c symmetry (denoted C2/c), and garnet (gt). Agreement of our calculated phase equilibria with available experimental data is excellent (Figure 1). The transitions from plagioclase- to spinel- to garnet-bearing assemblages agree well with experiments on the $\text{CaO-MgO-Al}_2\text{O}_3\text{-SiO}_2$ (CMAS) system [*Wood and Holloway*, 1984] and whole rock compositions [*Kinzler*, 1997]. We note that addition of Cr_2O_3 , a component that we have not considered, will increase the pressure of the transition between the spinel- to garnet-bearing assemblages [*Nickel*, 1986]. We find that addition of iron lowers the opx-C2/c boundary as compared with its experimentally observed position in the MgSiO_3 system [*Pacalo and Gasparik*, 1990], in accord with expectations based on the FeSiO_3 system [*Hugh-Jones et al.*, 1994]. The pressure-temperature trend of the olivine to wadsleyite coexistence region is slightly different from that found by *Katsura and Ito* [1989] but in excellent agreement with the Clapeyron slope found by *Morishima et al.* [1994] for the Mg end-member. *Morishima et al.* argue that the results of *Katsura and Ito* [1989] may be biased by inaccurate pressure-temperature calibration. The Mg-rich pyroxene-out boundaries are the most uncertain, in part because experimental constraints are few. The high-temperature stability of orthopyroxene, defined by the dashed curve, is probably overestimated due to our neglect of asymmetric Mg-Ca interactions in clinopyroxene. Our self-consistently computed phase diagram is very similar to the empirical diagrams compiled by *Ita and Stixrude* [1992] with the following notable exceptions: we have now included plagioclase, spinel, and C2/c Mg-rich pyroxene, which were not considered in the earlier study. The transitions among the olivine polymorphs show the same topology as that assumed by *Ita and Stixrude* [1992], but our phase equilibria are in better accord with experimental data: The dP/dT Clapeyron slopes of our self-consistent computations are greater, and olivine+ringwoodite coexistence is restricted to lower temperature than that assumed by *Ita and Stixrude* [1992].

[17] Agreement with available experimental data on phase proportions is good although there are some significant discrepancies (Figure 2). The fraction of cpx is underestimated by our computations in the pressure range 10–13 GPa. This is attributed to our neglect of Na and Al in cpx. The difference between computed and observed olivine fraction is attributed to (1) the slight difference in composition between the pyrolite composition adopted here and that of *Irfune and Isshiki* [1998] and (2) the slight difference between atomic fraction and volume fraction of olivine in pyrolite (<1%). The plagioclase-spinel-garnet facies reactions are increasingly buffered by aluminous enstatite with

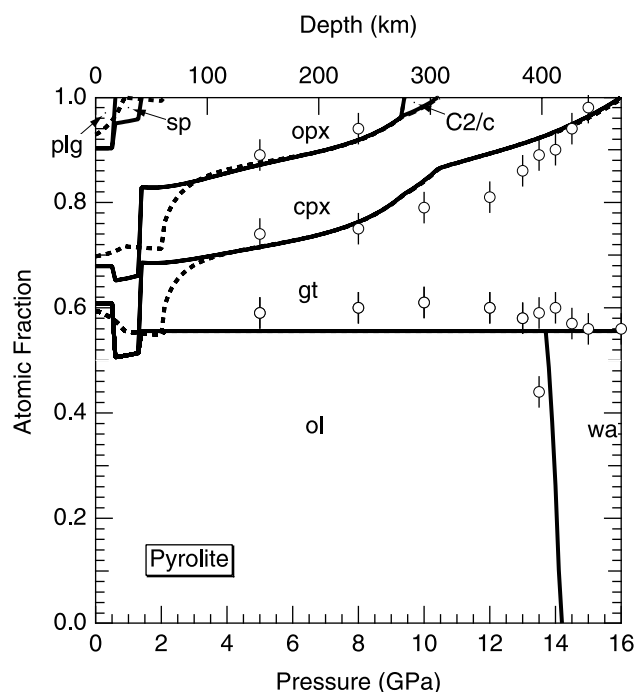


Figure 2. Phase proportions as atomic fraction computed along the 1600 K isentrope (dashed) and along a geotherm for 100 Ma oceanic lithosphere (solid) compared with volume fractions (symbols) computed via mass balance by Irifune and Isshiki [1998] from their experimental observations.

increasing temperature, resulting in lesser amounts of plagioclase and spinel, and more gradual variations in the amount of plagioclase, spinel, and garnet with depth [see also Green and Falloon, 1998]. These reactions are divariant in the CFMAS system under consideration but occur over a pressure interval of less than 0.1 GPa according to our calculations, in excellent agreement with the experiments of Robinson and Wood [1998].

3.2. Geotherm

[18] We assume an isentropic interior overlain by a lithosphere defined by the half-space conductive cooling solution (Figure 3). The isentropes are computed self-consistently by finding the $P - T$ path along which the total entropy of the assemblage is constant [Ita and Stixrude, 1992]; phase transformations produce kinks in the isentrope due to the exchange of latent heat [Verhoogen, 1965]. Most of our results are based on a potential temperature of 1600 K, which lies between two estimates of the potential temperature required to produce oceanic crust of average thickness [Klein and Langmuir, 1987; McKenzie and Bickle, 1988]. Over the depth range of interest, our 1600 K isentrope differs by less than 20 K from that of Ita and Stixrude [1992]. For the lithosphere, we also consider a continental geotherm from the Canadian shield (East Abitibi [Jaupart and Mareschal, 1999]).

3.3. Seismic Velocity of Individual Phases

[19] The variation of velocity with depth is typified by olivine: The velocity decreases with increasing depth in the

thermal boundary layer, and then increases with depth below the lithosphere, reflecting the influence of pressure on the shear modulus (Figure 4). The velocity rises rapidly with increasing depth at the limit of olivine stability as the iron content of olivine and wadsleyite both decrease with increasing pressure throughout the coexistence interval. The depth at which the velocity is minimum along the 100 Ma geotherm is similar for olivine (150 km), orthopyroxene (150 km), clinopyroxene (140 km), and garnet (150 km). The shear wave velocity of most other phases is also affected by variations in their composition with depth. The initial increase in shear wave speed with depth of orthopyroxene is not a robust feature of our calculations. This feature originates in a calculated enrichment in Fe in opx at the expense of olivine on cooling and is very sensitive at low temperatures (<800 K) to the form of nonideal Mg-Fe interactions in orthopyroxene, assumed to be absent here.

[20] In order to compare with previous work, we have computed the elastic properties of olivine along the 1400°C (1673 K) adiabat. Duffy and Anderson [1989] find a much stronger depth dependence of V_S along this adiabat than we find: Their value for V_S at 400 km is 2.5% higher than ours, and their value at 0 km depth is 1.5% lower than ours. The greater pressure dependence found in the earlier study can be traced to the assumed value of G'_0 . While Duffy and Anderson [1989] assumed $G'_0 = 1.8$, we and other recent modeling studies [Vacher et al., 1998] assume $G'_0 = 1.4 \pm$

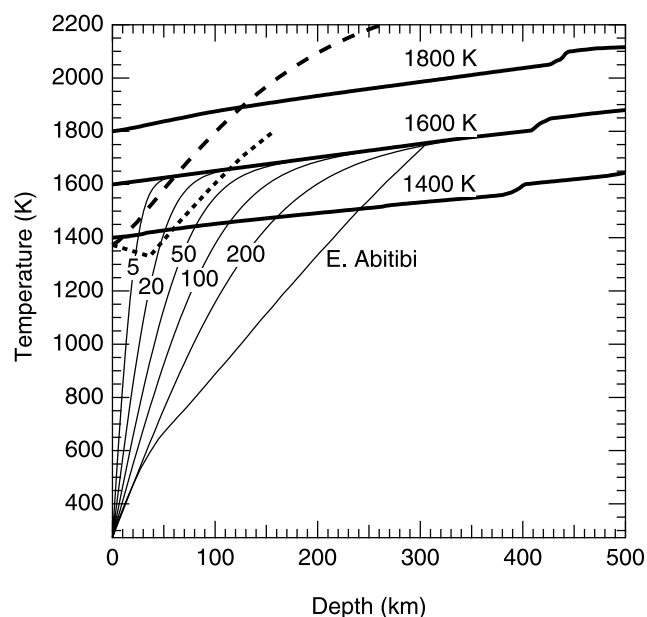


Figure 3. Computed isentropes with indicated potential temperatures (bold lines), oceanic thermal boundary layers (light lines) computed with the half-space cooling model for indicated lithospheric ages in millions of years, and the continental shield geotherm of Jaupart and Mareschal [1999] labeled “E. Abitibi.” The dry (long dashed) [McKenzie and Bickle, 1988; Zhang and Herzberg, 1994] and moist (short-dashed) [Hirth and Kohlstedt, 1996] ($H/Si = 810$ ppm) peridotite solidi are shown for comparison.

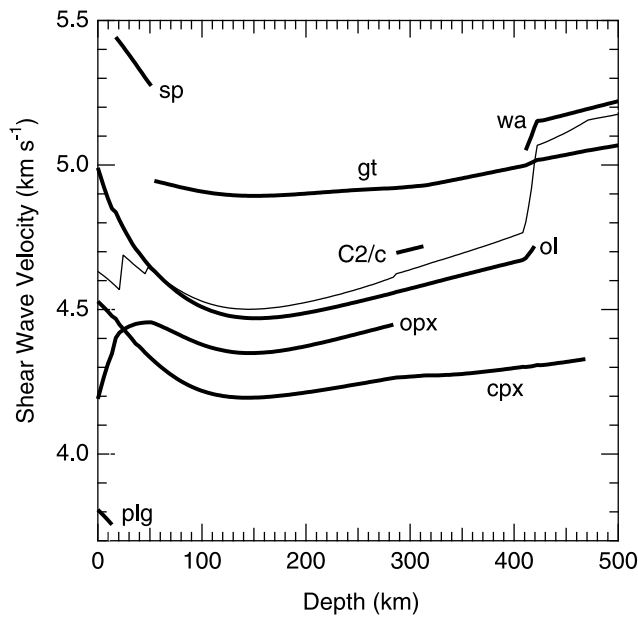


Figure 4. Shear wave velocity at infinite frequency of individual phases in pyrolite along the 100 Ma geotherm (bold) compared with the velocity of the aggregate (thin).

0.1 based on measurements that cover a much wider pressure range.

3.4. Seismic Velocities of the Aggregate: Null Hypothesis

[21] Our calculations show a distinct low-velocity zone along oceanic geotherms (Figures 5 and 6). The presence of an extremum appears to be robust when uncertainties in the computed velocities are considered. Considering uncertainties in thermodynamic parameters as outlined in the Figure 5 caption, we estimate the uncertainties in the aggregate shear wave velocity to be $\pm 1.3\%$ ($\pm 0.06 \text{ km s}^{-1}$), which is much greater than the difference between Voigt and Reuss extremal bounds ($\pm 0.3\%$) except within the plagioclase stability field where the very low velocity of this mineral leads to wide bounds ($\pm 1.3\%$).

[22] Our results for the shear wave velocity in the vicinity of the low velocity zone may be approximated by

$$V_S = 4.77 + 0.0380(P, z/29.80) - 0.000378(T - 300) \quad (7)$$

where V_S is in km s^{-1} , P is in GPa, and T is in K. The expression is valid at depths (pressures) between the garnet-in transition (near 50 km depth, 1.4 GPa) and the orthopyroxene to C2/c transition (near 285 km depth, 9.4 GPa). Over this range, the misfit between the approximate expression and our calculations is 0.006 km s^{-1} RMS for oceanic geotherms from 0 to 200 Ma. For the continental geotherm, the approximate expression systematically overestimates V_S by a maximum of 0.016 km s^{-1} . The temperature and pressure derivatives of the velocity represented by the coefficients in this expression are effective values that are averages over the relevant pressure and temperature range and which include the influence of pressure- and temperature-dependent phase transformations

(e.g., pyroxenes to garnet). The velocity evaluated according to (7) at ambient conditions (4.77 km s^{-1}) is consistent with the velocity of a suite of natural spinel and garnet peridotites calculated by Lee [2003] for the Mg # of our bulk composition (4.81 km s^{-1}).

[23] The effect of decreasing lithospheric age is to shift the low velocity zone to shallower depths and to decrease the value of the minimum velocity (Figure 7). The local minimum in the velocity may be characterized by the velocity deficit relative to ambient conditions

$$\Delta V_S = V_{S0} - V_{S\min} \quad (8)$$

where $V_{S0} = 4.77 \text{ km s}^{-1}$ is the velocity evaluated from the fit to our results (equation (7)) at ambient conditions and

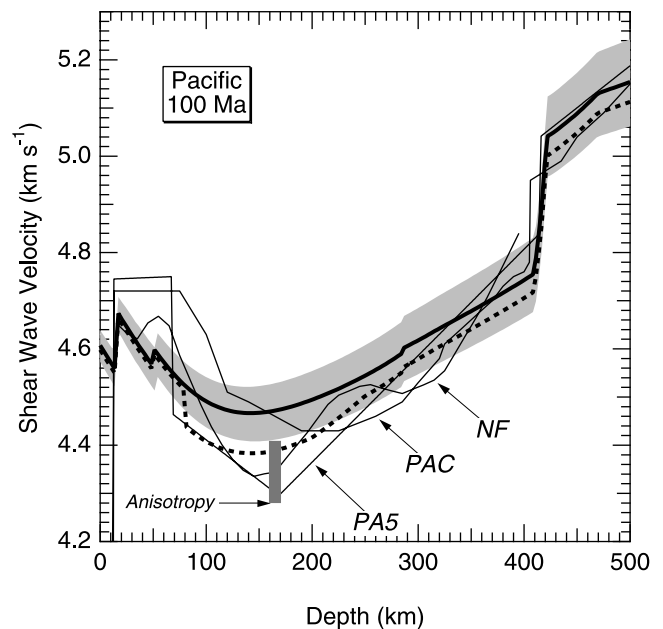


Figure 5. Shear wave velocity of the null hypothesis along the 100 Ma geotherm (bold line). Shading represents the uncertainty in the calculated velocity assuming uncertainties in G , G' , and dG/dT for each phase of $\pm 2 \text{ GPa}$, ± 0.1 , and $\pm 1 \text{ MPa K}^{-1}$, respectively. The bold dashed line shows the null hypothesis corrected for dispersion according to the attenuation model QR19 for 100 Ma Pacific [Romanowicz, 1995] and $\alpha = 0.25$. We have approximated the variation of attenuation with depth as $1000/Q(z) \approx 1000/Q_{00}(z) + 0.5$, as appropriate for 100 Ma Pacific [Romanowicz, 1998], where $1000/Q_{00}(z)$ is the spherically averaged value of the attenuation at depth z in QR19. Our calculations are compared with seismological models (light lines) PAC [Graves and Helmberger, 1988], NF110+ [Nishimura and Forsyth, 1989], and PA5 [Gaherty et al., 1999a]. For NF110+, we have calculated the Voigt-Reuss-Hill isotropic velocity from the five anisotropic parameters of the seismological model at each depth. For PA5, we have estimated the isotropic velocity as the simple average of SH and SV . PAC is an SH model which is the faster of the two S wave polarizations. The approximate magnitude of SH - SV anisotropy is indicated by the vertical bar.

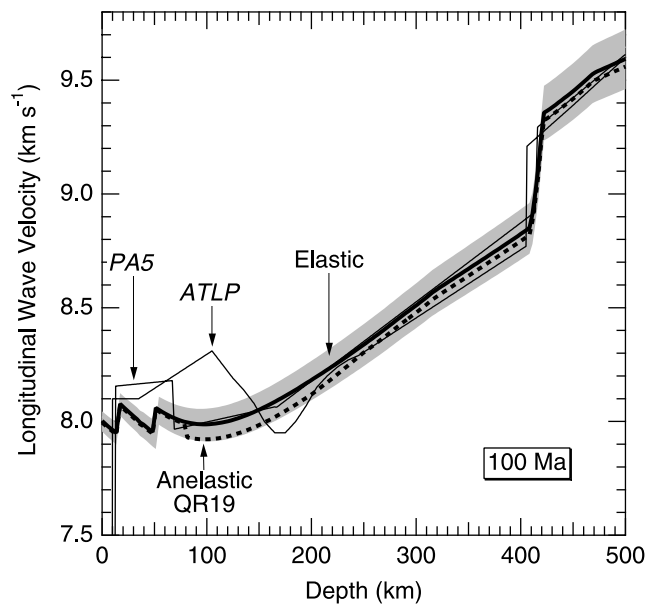


Figure 6. Comparison of the compressional wave velocity of the null hypothesis (bold with shading to indicate uncertainty) along the 100 Ma geotherm with that of seismological models (light lines) ATL P [Zhao and Helmberger, 1993] and PA5 [Gaherty et al., 1999a]. For PA5, we have estimated the isotropic velocity as the simple average of P_H and P_V . ATL P is a P_H model which is the faster of the two P wave propagation directions. The bold dashed line shows the null hypothesis corrected for dispersion according $Q_P = 9/4Q_S$ appropriate for a Poisson solid and no bulk attenuation, and Q_S is the same as that used in the shear wave dispersion calculation (Figure 5).

V_{Smin} is the minimum value of the velocity. The velocity deficit is approximated to within 0.01 km s^{-1} by

$$\Delta V_S = (1.63 + 0.16\sqrt{t})^{-1} \quad (9)$$

with t in units of Ma and V_S in units of km s^{-1} . The depth at which the minimum occurs, z_{min} decreases with decreasing lithospheric age: $z_{min} = 180 \text{ km}$ at 200 Ma and $z_{min} = 60 \text{ km}$ at 10 Ma.

[24] Below and above the low-velocity zone, the variation of velocity with depth is not smooth. Discontinuities near 10, 50, and 285 km depth are due to phase transformations from plagioclase- to spinel- and from spinel- to garnet-bearing assemblages, and from orthopyroxene to C2/c Mg-rich pyroxene, respectively. The depths of these discontinuities depend on temperature (Figure 1). The magnitude of the velocity discontinuities also depend on temperature and are largest along continental geotherms and old oceanic lithosphere.

[25] Our results differ substantially from the elastic wave velocity calculated in some previous studies of the origin of the low velocity zone. Along the same geotherm, the velocity of Birch [1969] and Schubert et al. [1976] are 0.12 km s^{-1} higher than ours while that of Karato and Jung [1998] fall more than 0.1 km s^{-1} below at depths of the velocity minimum. These differences fall well outside our estimated uncertainties. The differences arise from our more

complete model of mantle elasticity which, unlike these earlier studies, includes the nonolivine fraction and the most recent experimental data. The calculations of Birch [1969] were based on a semiquantitative guess at G' while those of Schubert et al. [1976] were based on G' from Kumazawa and Anderson [1969], which subsequent measurements over a wider pressure interval have shown to be overestimated by 25%. Karato and Jung [1998] appear to have adopted anomalous values of the pressure and temperature derivatives of V_S that are not supported by experiment.

[26] In order to compare with other studies of the shear wave velocity of multiphase mantle assemblages, we have computed the properties of pyrolite along the 1400°C (1673 K) adiabat. We find that our shear wave velocity differs by less than 0.5% from that estimated by Weidner [1985] from the solidus to 400 km depth. The excellent agreement is partly coincidental since our estimated uncertainty is greater than the difference and since at the time of Weidner's study temperature derivatives of the shear modulus were unknown for most mantle minerals. At 400 km our value of V_S is 3% smaller than that of Anderson and Bass [1984], which we attribute to better estimates of the pressure and temperature derivatives of the shear modulus based on more recent experimental data. Another possible source of discrepancy is that Anderson and Bass assumed that the relative proportions of olivine, garnet, and the pyroxenes were constant from 0 to 400 km depth (0–14 GPa) while experiments show that these vary considerably (Figure 2). Between 185 and 400 km depth, our computed bulk sound speed and density profiles agree to within 1% with those determined by Ita and Stixrude [1992]. Our computed aggregate velocities agree with those of Vacher et al. [1998] to within 1% at 400 km.

4. Comparison With Seismological Models

[27] The null hypothesis captures many important features of seismological models, including the presence of a

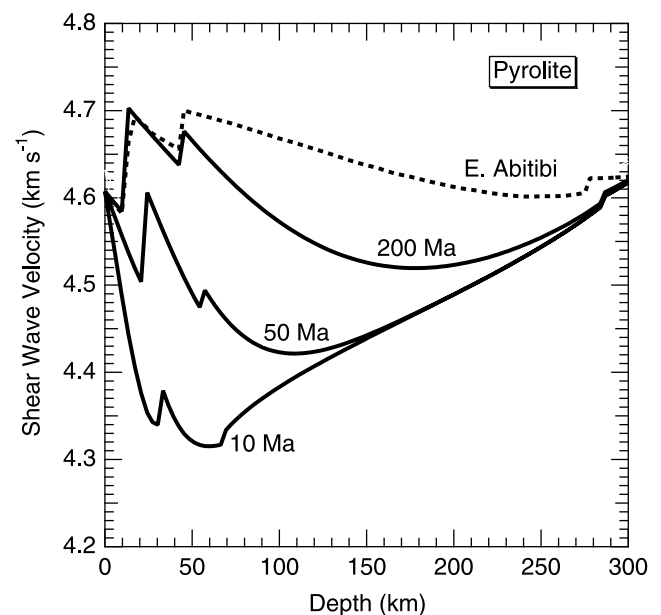


Figure 7. Influence of lithospheric age on the shear wave velocity. Velocity along a continental geotherm (dashed) is shown for comparison.

low-velocity zone of nearly the observed magnitude. In detail, the comparison reveals a small but apparently significant residual shear wave velocity deficit of 0.1–0.2 km s⁻¹ (Figure 5). The calculated value of the minimum velocity (4.47 km s⁻¹) is greater than that in the following models: 4.43 km s⁻¹ (PAC [Graves and Helmberger, 1988]), 4.34 (NNA80to135 [Nataf *et al.*, 1986]), 4.34 (NF110+ [Nishimura and Forsyth, 1989]), 4.29 (PA5 [Gaherty *et al.*, 1999a]), and 4.35 (S12-WM13 [Su *et al.*, 1994]), where the latter value is a path average for 100 Ma Pacific calculated by Gaherty *et al.* [1999a]. The calculated depth at which the minimum velocity occurs (145 km) is consistent within our computed uncertainties to that found in seismic models PA5 (166 km) and NF110+ (145) but is shallower than that found in PAC (208), NNA80to135 (220), and SM12-WM13 (220).

[28] Our calculated plagioclase- to spinel-facies transition has no plausible counterpart in seismological models. The mantle is likely to be depleted at the depth of this transition, which would tend to reduce the amount of plagioclase and spinel and the magnitude of the velocity discontinuity as compared with the null hypothesis. Moreover, the transition is known to be affected by elements such as Na and Cr, to the extent that the plagioclase facies may be absent along most geotherms [Wood and Yuen, 1983]. However, we caution that direct experimental observations of the transition, as opposed to thermodynamic calculations, are limited, especially at the low temperatures that are encountered along old oceanic, or continental geotherms.

[29] The Hales discontinuity, which occurs regionally near 60 km depth, cannot be explained by the spinel- to garnet-facies transition, as had been proposed [Hales, 1969], because the impedance contrast (product of density and velocity) is too small. The average value of the impedance contrast found by Revenaugh and Jordan [1991] for the Hales discontinuity is 7%, as compared with our calculated value of 1.5% for the spinel to garnet phase transformation. The small calculated contrast is consistent with previous calculations [Green and Liebermann, 1976] and with a suite of natural samples, which show no systematic difference in seismic velocity between garnet- and spinel-peridotites within the variance of bulk composition [Lee, 2003]. We note that other explanations have been offered for the Hales discontinuity under continents [Levin and Park, 2000].

[30] The null hypothesis has no counterpart to the Gutenberg (G) discontinuity [Revenaugh and Jordan, 1991]. The properties of the discontinuity are geographically variable, with an average impedance contrast of -6.6% and average depth of 66 km for oceanic regions away from island arcs. Relative to our results, the G discontinuity seems to be composed of a velocity deficit at z_G^+ and a velocity excess at z_G^- , where z_G is the depth of the discontinuity.

[31] The opx to C2/c transition occurs at a depth similar to that of the X discontinuity, which Revenaugh and Jordan [1991] find regionally at a depth near 300 km. In our calculations, the position of the phase transition is better constrained than the magnitude of the discontinuity since the shear modulus of the C2/c phase has not yet been measured. In any case, the discontinuity due to this phase transition should be small because the amount of opx at the transition is small, which may explain why the X is often

absent or not seen. Our results are thus compatible with previous suggestions that the opx-C2/c transition may cause the X discontinuity [Woodland, 1998]. Experimental measurement of the shear modulus of the C2/c phase is needed to further test this proposed link.

[32] We find no features that can be plausibly linked to the Lehmann discontinuity, a feature of many seismological models including PREM in which it is located at 220 km depth [Dziewonski and Anderson, 1981]. There are two possible explanations for this apparent discrepancy. The first possible explanation is that the Lehmann is not a global feature. Recent studies have found that the Lehmann is more prevalent under continents and that it may be absent under all or most of the oceans [Gu *et al.*, 2001; Gung *et al.*, 2003]. Tomographic models that use PREM as a reference inherit the Lehmann discontinuity, and as a result tend to locate the depth at which the velocity is minimum at 220 km [e.g., Su *et al.*, 1994]. The second possible explanation is that the Lehmann is in fact present under oceans, but has a cause that lies beyond the scope of the null hypothesis. Several studies have suggested that the Lehmann is caused by a rapid change in anisotropy [Gaherty and Jordan, 1995; Gung *et al.*, 2003].

[33] The magnitude of the shear wave velocity gradient below the low velocity zone differs significantly between the null hypothesis and most seismological models. Average shear wave velocity gradients in seismological models over the depth range between the velocity minimum and the 410 discontinuity (150–400 km) are for PA5, 2.19 mHz (i.e., m s⁻¹ km⁻¹); for ATLS, 1.80 mHz; for PREM, 1.94 mHz (including a Lehmann of 0.23 km s⁻¹ at 220 km); for TNA, 1.76 mHz; for NNF110+, 2.02; for PAC, 1.94 mHz, as compared with our calculated value for the 100 Ma geotherm, 1.10 mHz. On the other hand, the predicted velocity agrees very well with seismological models at the top of the transition zone. This is because in the seismological models, the effect of the greater velocity gradient is almost exactly balanced by a diminished 410 km discontinuity. As a result, the velocity gradient averaged over a slightly wider depth interval (145–450 km) is very similar between our predictions and seismological models.

[34] Is the high-gradient zone a robust feature of seismological models? The difference between the null hypothesis and seismological shear velocity models appears to be a tradeoff between the magnitude of the velocity gradient and the magnitude of the 410 km discontinuity. Recent calculations show that a 410 with a velocity change similar to ours and substantially larger than that in many seismological models agrees well with seismic reflectivity data [Gaherty *et al.*, 1999b]. It may be useful to explore the effects of trading off gradient and discontinuity magnitudes in the construction of seismological models [Kennett, 1991], possibly using the null hypothesis we present here as a starting point for hypothesis testing.

[35] Our calculated compressional wave velocity agrees very well with most features of seismological models, including the value of the minimum velocity, the depth at which the minimum occurs, and the velocity gradient below the low-velocity zone (Figure 6). As with the shear wave velocity, there are differences in the discontinuity structure and the comments that we have made regarding the shear

Table 2. Origin of the Residual Velocity Deficit of -0.1 to -0.2 km s $^{-1}$ for 100 Ma

Cause	Effect, km s $^{-1}$
Dispersion $1000/Q = 16-20$	-0.07 to -0.14
Temperature $\Delta T = 100$ K	-0.038
Iron content $\Delta X_{\text{Fe}} = 0.02$	-0.030
Partial melt 0.2% (direct effect only)	-0.02 to -0.07

wave discontinuities apply equally to those in the compressional velocity.

5. Discussion

[36] We focus our attention on the differences between the null hypothesis and seismological models that are most directly related to the origin of the low-velocity zone: the residual velocity deficit (Table 2), the G discontinuity (Table 3), and the high-gradient zone (Table 4). In order to account for these discrepancies, we explore variants of the null hypothesis, including modifications of the assumed major element composition and temperature profile. We also consider factors that go beyond the scope of the null hypothesis including the effects of partial melt, attenuation, and anisotropy.

5.1. Chemical Composition

[37] Variations of the bulk composition within a plausible range are unlikely to change the velocity by more than our calculated uncertainties. Addition of less abundant components, such as Na $_2$ O, TiO $_2$, Cr $_2$ O $_3$, and H $_2$ O is also unlikely to significantly affect the elastic velocity. The most important influence of these components will be on the position of phase transformations, for example the influence of Cr on the pressure of the spinel- to garnet-facies transition, as we have discussed. The possible influence of water on attenuation, which is unquantified, will be discussed further below. To illustrate the effect of variations in major element composition, we have computed the effect of an increase in the iron number $X_{\text{Fe}} = \text{Fe}/(\text{Fe} + \text{Mg})$ by 0.02. The decrease in the velocity is 0.030 km s $^{-1}$. The compositional derivative $dV_S/dX_{\text{Fe}} = -1.52$ km s $^{-1}$ is consistent with that found by Lee [2003] which, when reexpressed in terms of our compositional variable is -1.43 ± 0.09 km s $^{-1}$.

[38] To illustrate the influence of other compositional variables, and of compositional heterogeneity in the mantle, we have computed the velocity of other bulk compositions that may be representative of portions of the mantle (Table 1 and Figure 8). Along the 100 Ma geotherm, harzburgite shows a local minimum in the shear wave velocity at a similar depth to that found in pyrolite. The velocity of harzburgite is slightly higher than pyrolite throughout the

Table 4. Origin of the High Gradient Zone in V_S at 1.76–2.19 mHz a

Model	Result, mHz
Null	1.10
Null plus dispersion	1.3
Null (isotherm)	1.24
Null +0.2% (150 km) to 0% (400 km) partial melt (direct effect only)	1.2–1.4
0% (150 km) to 100% (400 km) pyroxenite	1.9

a Calculations for 100 Ma geotherm.

upper mantle. The depleted composition yields discontinuities associated with spinel phase transformations that are muted in comparison with pyrolite, and accentuated discontinuities associated with the orthopyroxene-C2/c and olivine to wadsleyite transitions.

[39] We consider the effect of depletion on the seismic velocity at the base of our calculated spinel-facies field, in which melting is thought to initiate [Robinson and Wood, 1998]. We find that pyrolite is 0.1 km s $^{-1}$ slower and 0.02 g cm $^{-3}$ denser than harzburgite along the 100 Ma geotherm. The difference in impedance is 1%, or 1/7 of the average impedance contrast of the G discontinuity. The boundary between pyrolite and harzburgite compositions may be gradual, with the amount of depletion increasing with decreasing depth. The depth range over which depletion occurs will influence the extent to which a change in composition may contribute to seismic reflectivity.

[40] Another type of major element heterogeneity that has been proposed in the upper mantle is the widespread presence of small amounts of pyroxenite [Hirschmann and Stolper, 1996]. Pyroxenite has an unusually high

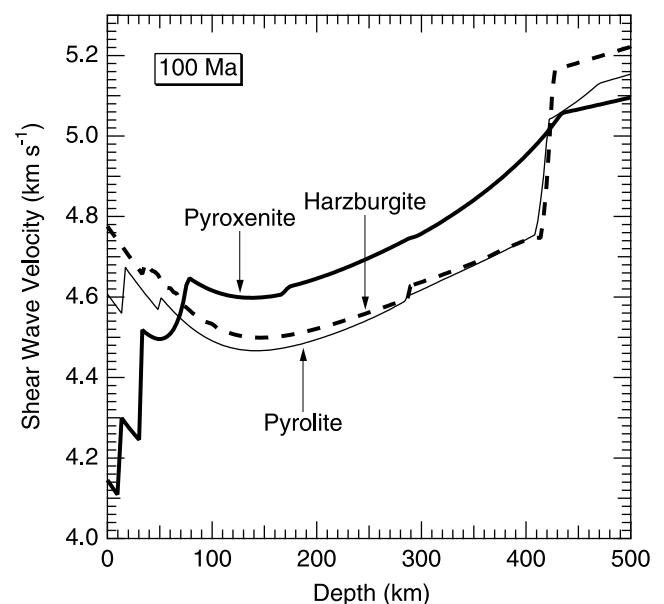


Figure 8. Influence of bulk composition on the shear wave velocity. Results for three bulk compositions are shown (Table 1) along the 100 Ma geotherm. Velocity discontinuities in pyrolite and harzburgite are discussed in the text. In pyroxenite, rapid changes in the velocity gradient occur near 10 km (plg- to sp-facies), 30 km (sp- to gt-facies), 80 km (plg out), 170 km (sp out), and 440 km (cpx out).

Table 3. Origin of the Gutenberg Discontinuity at -6.6% Impedance Contrast a

Cause	Effect (%)
Change in dispersion $\Delta 1000/Q = 9-13$	-0.9 to -2.0
Harzburgite to pyrolite	-1.0
Change in anisotropy $\Delta \xi = 0.06$	-1.5
Change in partial melt 0.2% (direct effect only)	-0.4 to -1.5

a Revenaugh and Jordan [1991].

velocity at depths greater than 80 km, because of its greater garnet content. If the amount of pyroxenite in the mantle were to increase systematically with depth, the velocity gradient would be greater than what we have found for the null hypothesis. A gradient in pyroxenite content may then help to resolve the large difference in velocity gradient between the null hypothesis and seismological models. To illustrate, we consider an extreme, end-member case: with 100% pyrolite and no pyroxenite at 150 km depth, grading to 100% pyroxenite at 400 km depth, the gradient is increased to 1.9 mHz. Is a systematic variation in pyroxenite content with depth in the upper mantle dynamically plausible? The answer to this question will likely require a better understanding of the origin of pyroxenite and of thermochemical convection.

5.2. Temperature Profile

[41] In order to account for uncertainties in mantle potential temperature, and in the lithospheric geotherm, we have considered the influence on the velocity of changing the temperature by 100 K. The approximate relation (equation (7)) shows that the mean change in the elastic shear wave velocity over the oceanic low velocity zone is $0.038 \pm 0.003 \text{ km s}^{-1}$.

[42] We have also considered a nonadiabatic sublithospheric geotherm, since the average temperature profile need not be adiabatic in the presence of spherical geometry [Jeanloz and Richter, 1979], internal heating [Jeanloz and Morris, 1987; Bunge et al., 2001], or phase transformations [Christensen, 1995]. To illustrate the effects at one extreme of what might be plausible, we have computed the velocity along the 1600 K isotherm. This has the effect of steepening the velocity gradient below the low-velocity zone as compared with the isentropic case by 13%, to 1.24 mHz, which is still substantially less than that found in seismological models.

5.3. Partial Melt

[43] The presence of partial melt has often been invoked to account for the properties of the low-velocity zone [Lambert and Wyllie, 1968; Anderson and Sammis, 1969; Ringwood, 1969; Green and Liebermann, 1976; Sato et al., 1989]. Partial melting in the depth range of the low velocity zone is expected within the moist melting regime (also called incipient, damp, water assisted or vapor present) that lies below the dry solidus (Figure 3). The amount of partial melt that is produced in this regime is not well quantified experimentally, is probably very small, but nevertheless is potentially significant for explaining certain geochemical anomalies in mid-ocean ridge basalts [Plank and Langmuir, 1992; Hirth and Kohlstedt, 1996]. It is not possible at present to estimate with any certainty how much partial melt remains at depth for geologically long periods of time or what its influence on seismic wave velocities may be.

[44] For the estimate of the moist solidus that we have adopted [Hirth and Kohlstedt, 1996], partial melt is unstable and will refreeze for lithospheric ages older than approximately 40 Ma. Partial melt could then contribute to the residual velocity deficit throughout most of the oceanic upper mantle only if 1) the water content in the low-velocity zone is greater than has been assumed 2) the moist solidus for a given water content lies at lower temperatures than has

been assumed or 3) the mantle temperature is higher than we have assumed. The stability field of melt in the asthenosphere is still highly uncertain. Models of the moist peridotite solidus rely primarily on experimental measurements of the dry and water-saturated end-members. The amount of water that is assumed to exist in the upper mantle is also poorly constrained [Hirth and Kohlstedt, 1996]. Other volatile constituents, such as CO_2 may also influence the solidus [Taylor and Green, 1988].

[45] Assuming that a small degree of partial melt is thermodynamically stable, and that it can remain at depth for geologically significant periods, two different effects of partial melt on the seismic wave velocity must be distinguished: the direct effect due to the contrast in elastic properties between melt and solid and the indirect effect via the influence of partial melt on attenuation and dispersion. The indirect effect, which is unquantified in the seismic band, will be discussed further below. If we assume a melt fraction of 0.2% in the low-velocity zone [Plank and Langmuir, 1992], the direct effect reduces the shear wave velocity by $0.02\text{--}0.07 \text{ km s}^{-1}$ [Hammond and Humphreys, 2000], with the uncertainty due primarily to unknown partial melt geometry. The direct effect of partial melt can then account for 10–70% of the residual velocity deficit. We may also envision that a contrast in the amount of partial melt contributes to the Gutenberg discontinuity. If we neglect the change in density upon partial melting, and assume that the mantle contains 0.2% partial melt below the discontinuity and none above, then the impedance contrast between unmelted and partially molten mantle is 0.4–1.6%, or 1/16–1/4 of the average impedance contrast of the G discontinuity. Partial melt may also influence the velocity gradient. If we assume 0.2% partial melt at 150 km, decreasing to 0% at 400 km, the average velocity gradient over this depth range would be 10–30% larger than that of the null hypothesis, or 1.1–1.3 mHz, still substantially less than that in most seismological models.

5.4. Attenuation and Dispersion

[46] We find that dispersion can account for most to all of the residual velocity deficit. Attenuation of seismic waves is known to be particularly high in a depth range that is similar to that of the low-velocity zone. Attenuation entails dispersion so that the seismic wave velocity at finite frequency is less than in the elastic limit. The magnitude of the attenuation is uncertain. Because of this uncertainty, we maintain dispersion as a distinct contribution to the velocity in our discussions of upper mantle structure in Tables 2–4.

[47] We use seismological models as our sole source of information on the value of the attenuation in the low-velocity zone. A disadvantage of our approach is the large uncertainty and limited spatial resolution of seismological attenuation models as compared with velocity models [Romanowicz and Durek, 2000]. We believe that these uncertainties are outweighed by our current inability to estimate securely the attenuation of mantle assemblages at the relevant conditions on the basis of laboratory experiments. While the effect of temperature and frequency on the attenuation have been measured experimentally [Jackson et al., 2002], the effect of pressure, partial melt, and water are unquantified in the seismic band, although speculative models have been proposed for the latter [Karato and Jung,

1998]. Our approach therefore does not help to constrain the physical mechanism that produces the high attenuation in the low-velocity zone; indeed, the experimental data needed to identify the mechanism do not yet exist. This is an important point in considerations of the origin of the high-attenuation zone. Dispersion in our analysis does not exclude, and may in fact require, an enhancement of attenuation via partial melt or trace amounts of hydrogen. By the same token, we can not exclude the possibility that partial melt and hydrogen play no significant role and that high attenuation occurs in the solid state as the result of variation of pressure and temperature at the base of a thermal boundary layer. Indeed, *Jackson et al.* [2002] have argued that attenuation in the low-velocity zone is consistent with that of dry, melt-free samples.

[48] In the low-attenuation limit dispersion is given by [*Anderson, 1989*]

$$1 - \frac{V(P, T, \omega)}{V(P, T, \infty)} = \frac{1}{2} \cot\left(\frac{\alpha\pi}{2}\right) Q^{-1}(P, T, \omega) \quad (10)$$

The relationship between this expression and more complete rheological models is discussed by *Jackson et al.* [2002]. An important feature of this equation, which does not hold outside of the small attenuation limit, is that dispersion depends on pressure, temperature, and frequency only through their effect on the attenuation Q^{-1} . The factor multiplying the attenuation has a value near unity for typical values of the frequency exponent α (1.21 for $\alpha = 0.25$).

[49] We find velocity reduction due to dispersion of $0.07\text{--}0.14 \text{ km s}^{-1}$, based on a range of $1000/Q = 16\text{--}20$, and $\alpha = 0.2\text{--}0.3$ that are consistent with seismological attenuation models of the low-velocity zone [*Gaherty et al.*, 1999a; *Romanowicz, 1995*], and experimental results [*Jackson et al.*, 2002], respectively. Within uncertainties, agreement between the null hypothesis with dispersion and a range of seismological velocity models of 100 Ma Pacific is good at depths greater than 65 km for V_S and V_P (Figures 5 and 6). Moreover, the calculated minimum shear wave velocity falls within the range of seismological models at all ages, although the agreement with the model of *Nataf et al.* [1986] and *Su et al.* [1994] is much better than that with the models of *Nishimura and Forsyth* [1989] and *Gaherty et al.* [1999a] (Figure 9). An exception is in the immediate vicinity of the ridge ($<5 \text{ Ma}$) where very low velocities, as low as 3.7 km s^{-1} (SV) [*Webb and Forsyth, 1998*] probably cannot be explained by the null hypothesis with dispersion, and may require the direct effect of partial melt in amounts much larger than we have considered above, i.e., a few percent.

[50] We find that a rapid decrease in attenuation near 65 km depth cannot account for the Gutenberg discontinuity (Figure 5). Considering a range of global and regional models, which show attenuation contrasts near 65 km depth $\Delta(1000/Q) = 9\text{--}13$ [*Romanowicz and Durek, 2000*], and a range of $\alpha = 0.2\text{--}0.3$, we find that the resulting change in velocity is $0.04\text{--}0.09 \text{ km s}^{-1}$, or $1/7$ to $1/3$ of the average impedance contrast of the G discontinuity. Our analysis is thus inconsistent with the conclusions of *Karato and Jung* [1998], who argued that the Gutenberg discontinuity was caused primarily by a change in attenuation. Indeed, the calculations of *Karato and Jung* [1998] show a velocity

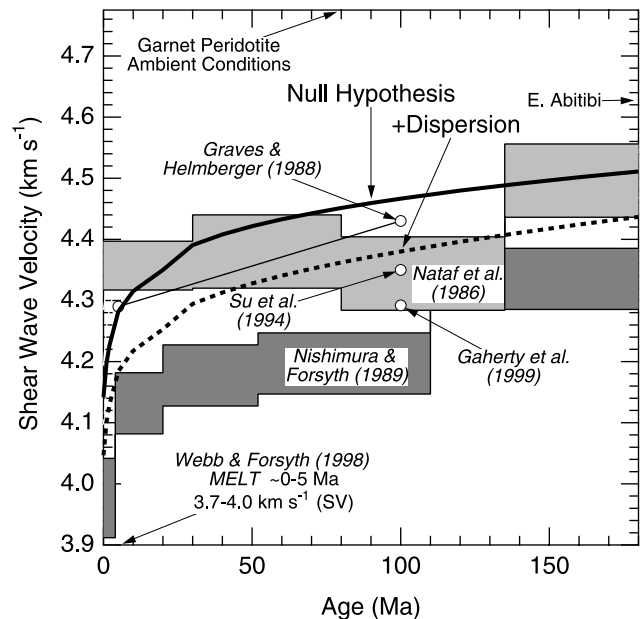


Figure 9. Minimum value of the velocity as a function of lithospheric age in the null hypothesis (bold solid) and the null hypothesis (bold dashed) corrected for dispersion according to the attenuation model QR19 [*Romanowicz, 1995*]. The values shown for *Nataf et al.* [1986] (light shading) and *Nishimura and Forsyth* [1989] (dark shading) are the Voigt-Reuss-Hill isotropic velocity computed from the five anisotropic parameters of the seismological models. For PA5 (symbol, *Gaherty et al.*, 1999a) we have estimated the isotropic velocity as the simple average of SH and SV . For S12-WM13 (symbol, *Su et al.* [1994]) the value is a path average for 100 Ma Pacific computed by *Gaherty et al.* [1999a]. Following the suggestion of *Graves and Helmberger* [1988] (PAC), we have indicated (symbols connected by light solid line) a smooth variation between their model of old Pacific and model TNA of *Grand and Helmberger* [1984]. PAC is an SH model, which is the faster of the two S wave polarizations. Also indicated are the minimum velocity along a continental geotherm (E. Abitibi), the velocity of garnet peridotite at ambient conditions, and the systematic variation of minimum SV velocities with lithospheric age determined in a high-resolution study of the first 5 Myr west of the East Pacific Rise [*Webb and Forsyth, 1998*]. The variation of attenuation with lithospheric age t (in units of Ma) in the low-velocity zone is approximated as $1000/Q \approx 16 + 3(1 - t/100)$ as appropriate for the Pacific [*Romanowicz, 1998*].

discontinuity that is very small compared with the magnitude of the G discontinuity.

[51] The decrease in attenuation with increasing depth below the high attenuation zone tends to increase the calculated shear wave velocity gradient as compared with the null hypothesis, but not sufficiently to account for the high-gradient zone as seen in seismological models. Seismological attenuation models show a rapid decrease in attenuation at the base of the high-attenuation zone in the range $160\text{--}250 \text{ km}$ depth, depending on the attenuation model. The average gradient between 150 and 400 km in the null hypothesis with dispersion from the spherically

averaged part of QR19 is 1.3 mHz, 20% larger than the elastic limit. In some seismic models the attenuation decreases rapidly at a depth similar to that of the Lehmann discontinuity, which may contribute to the velocity contrast associated with this feature.

5.5. Anisotropy

[52] A complete exploration of anisotropy lies beyond the scope of this study. However, we note that our method is sufficiently general to encompass anisotropic properties via computation of the full elastic constant tensor (equation (3)). Here, we restrict ourselves to an illustrative calculation of the possible contribution of anisotropy to the G discontinuity as suggested by *Gung et al.* [2003]. We can estimate the possible contrast in SV by assuming an isotropic mantle shallower than 65 km, and anisotropy of a magnitude typical of seismological models below 65 km. The relevant seismological quantity is $\xi = (V_{SH}/V_{SV})^2$ which is ≈ 1.06 in the model of *Nishimura and Forsyth* [1989] over a wide depth range for lithospheric age >20 Ma. The contrast in SV is then approximately $V_S(\xi - 1)/4 = 0.07 \text{ km s}^{-1}$ or 1.5%, which is 1/4 of the observed average impedance contrast for the G discontinuity.

6. Conclusions

[53] We have presented a new method with which it is now possible to construct mineralogical models of the upper mantle that account self-consistently for the relevant phase equilibria and physical properties including the seismic wave velocities. Consideration of both phase equilibria and seismic wave velocities is important, particularly in the upper mantle where phase transitions occur throughout and the seismic velocities of phases differ substantially. Thermodynamic self-consistency allows us to specify the problem with a minimum number of parameters and to take maximal advantage of the multiple redundancy of experimental observations.

[54] Our models form the basis of a null hypothesis that is now experimentally and theoretically well defined and provides a basis of comparison with seismological models and for understanding the origin of the low-velocity zone. Remaining uncertainties in the shear and compressional wave velocities of the null hypothesis are about 1%. Further progress in quantification of the null hypothesis is important and is readily accommodated by our method through the incorporation of other chemical components, computations of the full elastic constant tensor for investigations of anisotropic structure, and from further experimental advances, particularly in the measurement of elastic moduli that are currently unknown and better constraints on phase equilibria.

[55] Our results indicate that a solid-state low-velocity zone can account for most seismic observations. A low-velocity zone of nearly the observed magnitude is the natural consequence of a thermal boundary layer and the effects of pressure and temperature on the elastic wave velocity of subsolidus mantle assemblages. Dispersion has a secondary effect and is important for providing a quantitative explanation of the minimum velocities. Other factors can lead to further reductions in the velocity, but none of these seem to be required to explain seismological models, except in the immediate vicinity of the ridge. This is in

contrast to many previous studies that invoked widespread melt but did not have the advantage of experimental data at the relevant pressure, or a self-consistent thermodynamic model of the multiphase mantle. As many other variables that might have been relevant are apparently not required to explain the low-velocity zone, our picture focuses attention on the origin of the enhanced dispersion of this region. *Jackson et al.* [2002] argue tentatively that the enhanced dispersion is consistent with that of essentially dry, melt-free samples, which would mean that neither partial melt nor water play a significant role for either the velocity or the attenuation. Further elucidation of the origins of the high attenuation in the low velocity zone will come from experimental measurements of the effect of partial melt [*Jackson et al.*, 2004], pressure, and water content, and other variables on attenuation and dispersion within the seismic band.

[56] If partial melt exists globally in the low-velocity zone, it must be “hidden”, that is invisible to the seismological models to which we have compared. Partial melt might be hidden if it occurs in amounts that are so small that they do not significantly influence seismic wave velocities. The amount permissible by our analysis is a few tenths to 1% depending on melt geometry, the magnitude of the residual velocity deficit, and the value of Q . For example, if the model of *Gaherty et al.* [1999a] is more representative of the low-velocity zone than other models, more partial melt would be permissible, though still not required. The distribution of partial melt in the low-velocity zone need not be homogeneous. Partial melt in excess of 1% could be invisible if it were distributed heterogeneously with a characteristic length scale much less than that of a seismic wave. Our analysis suggests that experimental studies of phase equilibria of water-undersaturated assemblages may be able to place tighter constraints on the amount of partial melt. At least one current estimate of the moist solidus indicates that partial melt is not thermodynamically stable throughout most of the oceanic low velocity zone.

[57] Other features of upper mantle structure are more difficult to explain, including the Gutenberg discontinuity. Several factors that are all plausibly linked to the extraction of partial melt and depletion may contribute: a change in major element composition, a change in anisotropy, and a rapid increase in attenuation. However, neither of these factors alone or in combination appear to be sufficient to explain the magnitude of the impedance contrast.

[58] The very large shear wave velocity gradient seen in seismological models below the low-velocity zone is also difficult to explain. A subadiabatic thermal gradient, decreasing attenuation or partial melt with depth, and experimental uncertainties appear to be insufficient explanations. We have suggested that a depth dependent increase in the amount of pyroxenite could produce an enhanced velocity gradient, but this is highly speculative in the absence of a plausible dynamical picture. Moreover, any explanation for the discrepancy in shear wave velocity gradient must account for the essentially perfect agreement in the compressional velocity gradient between null hypothesis and seismological models.

[59] Discovery of the origin of the G discontinuity and the high gradient zone is frustrated to some extent by the fact that comparisons are not to seismological observations, but to seismological models, which are nonunique. One

Table A1. Properties of Mantle Species^a

Phase	Species	Formula	F_0 , kJ mol ⁻¹	V_0 , cm ³ mol ⁻¹	K_0 , GPa	K'_0	θ_0 , K	γ_0	q	G_0 , GPa	G'_0	η_{S0}	References ^b
Feldspar (plg)	anorthite	CaAl ₂ Si ₂ O ₈	-235.0	100.79	84	4.0	753	0.46	1.0	40	0.5	2.2	1–7
Spinel (sp)	spinel	(Mg ₃ Al ₁)(Al ₇ Mg ₁)O ₁₆	-148.0	158.84	197	4.0	869	1.27	1.0	108	0.4	2.5	1–3, 7–9
Spinel	hercynite	(Fe ₃ Al ₁)(Al ₇ Fe ₁)O ₁₆	-35.0	163.37	197	4.0	721	1.27	1.0	85	0.4	2.5	3, 10–12
Olivine (ol)	forsterite	Mg ₂ SiO ₄	-114.1	43.67	129	4.2	814	1.14	1.9	82	1.4	2.0	8, 13–20
Olivine	fayalite	Fe ₂ SiO ₄	-81.1	46.27	127	5.2	619	1.08	1.9	51	1.4	1.1	3, 13, 19, 21, 22
Wadsleyite (wa)	Mg-wadsleyite	Mg ₂ SiO ₄	-86.5	40.52	174	4.0	858	1.32	1.6	112	1.5	2.4	13–19, 23–25
Wadsleyite	Fe-wadsleyite	Fe ₂ SiO ₄	-71.8	43.22	174	4.0	671	1.32	1.6	72	1.5	2.4	13, 19, 23–26
Ringwoodite (ri)	Mg-ringwoodite	Mg ₂ SiO ₄	-76.9	39.65	183	4.1	891	1.21	2.0	119	1.3	2.3	3, 13–19, 27–29
Ringwoodite	Fe-ringwoodite	Fe ₂ SiO ₄	-72.7	42.02	192	4.1	671	1.21	2.0	105	1.3	2.3	13, 19, 24, 28, 30
Orthopyroxene (opx)	enstatite	Mg ₂ SiO ₄	-316.0	125.32	106	9.0	818	0.92	2.0	77	1.5	2.1	3, 13–19, 31–36
Orthopyroxene	ferrosilite	Fe ₂ SiO ₄	-257.3	131.84	101	9.0	689	0.98	2.0	52	1.5	2.1	3, 19, 34–37
Orthopyroxene	Mg-Tschermak's	(Mg ₂ Al ₂)Si ₂ Al ₂ O ₁₂	-121.6	120.50	106	9.0	818	0.92	2.0	106	1.5	2.1	1, 36, 38
C2/c (C2/c)	Mg-C2/c	Mg ₄ Si ₄ O ₁₂	-297.6	121.72	116	4.5	836	0.92	1.6	86	1.5	2.1	13–18, 39
C2/c	Fe-C2/c	Fe ₄ Si ₄ O ₁₂	-251.1	127.88	110	5.0	712	0.98	1.6	68	1.5	2.1	37, 40
Clinopyroxene (cpx)	diopside	Ca ₂ Mg ₂ Si ₄ O ₁₂	-516.4	132.22	114	4.5	785	1.06	1.6	67	1.2	2.1	2, 3, 19, 41, 42
Clinopyroxene	hedenbergite	Ca ₂ Fe ₂ Si ₄ O ₁₂	-454.9	135.68	120	4.5	702	0.95	1.6	61	1.2	2.1	3, 19, 43, 44
Clinopyroxene	Mg-diopside	Mg ₂ Mg ₂ Si ₄ O ₁₂	-305.7	125.32	114	4.5	814	1.06	1.6	78	1.2	2.1	17, 45
Garnet (gt)	pyrope	Mg ₃ Al ₁ Al ₁ Si ₃ O ₁₂	-234.1	113.19	170	4.0	828	1.24	1.3	93	1.4	0.8	2, 8, 19, 46–48
Garnet	almandine	Fe ₃ Al ₁ Al ₁ Si ₃ O ₁₂	-195.0	115.23	177	4.0	740	1.04	1.3	97	1.4	0.8	3, 12, 19, 49, 50
Garnet	grossular	Ca ₃ Al ₁ Al ₁ Si ₃ O ₁₂	-461.0	125.30	168	4.5	817	1.05	0.3	109	1.1	2.5	3, 8, 19, 32, 49–51
Garnet	majorite	Mg ₃ Mg ₁ Si ₁ Si ₃ O ₁₂	-204.1	114.57	160	4.5	828	1.24	1.3	87	1.4	0.8	11, 17, 19, 47, 52–54

^aItalics indicate estimated values.^bReferences are 1, Wood and Holloway [1984]; 2, Robie et al. [1978]; 3, Bass [1995]; 4, Angel [1988]; 5, Fei [1995]; 6, Mueller et al. [2002]; 7, Knittle [1995]; 8, Anderson and Isaak [1995]; 9, Yoneda [1990]; 10, Jamieson and Roeder [1984]; 11, Smyth and McCormick [1995]; 12, Anovitz et al. [1993]; 13, Katsura and Ito [1989]; 14, Morishima et al. [1994]; 15, Suzuki et al. [2000]; 16, Ito and Takahashi [1989]; 17, Gasparik [1990]; 18, Pacalo and Gasparik [1990]; 19, Ita and Stixrude [1992]; 20, Zha et al. [1996]; 21, Robie et al. [1982]; 22, Graham et al. [1988]; 23, Fei et al. [1992]; 24, Sinogeikin et al. [1998]; 25, Li et al. [2001]; 26, Li and Liebermann [2000]; 27, Meng et al. [1993]; 28, Sinogeikin et al. [2001]; 29, Jackson et al. [2000]; 30, Fei et al. [1991]; 31, Hugh-Jones and Angel [1997]; 32, Thieblot et al. [1999]; 33, Zhao et al. [1995]; 34, Jackson et al. [1999]; 35, Flesch et al. [1998]; 36, Chai et al. [1997]; 37, Hugh-Jones et al. [1994]; 38, Skinner and Boyd [1964]; 39, Angel et al. [1992]; 40, Akimoto and Syono [1970]; 41, Krupka et al. [1985]; 42, Zhao et al. [1998]; 43, Kim et al. [1991]; 44, Haselton et al. [1987]; 45, Tribaudino et al. [2001]; 46, Tequi et al. [1991]; 47, Wang et al. [1998]; 48, Sinogeikin and Bass [2000]; 49, Irifune [1993]; 50, Wang and Ji [2001]; 51, Conrad et al. [1999]; 52, Pacalo and Weidner [1997]; 53, Downs and Bukowinski [1997]; 54, Sinogeikin and Bass [2002].

might envision using our models in two ways to overcome this limitation: (1) testing directly against seismological data by computing seismological observables from the mineralogical model (computation of travel times, and surface wave dispersion from, e.g., the null hypothesis augmented by attenuation, crustal structure, sediments, and ocean is in principle straightforward, but beyond the scope of this paper) and (2) using mineralogical models as a starting point for exploring the range of seismological models that match the data equally well, i.e., the null space of the inverse problem. The upper mantle is exceptionally complex with a large number of discontinuities, strong anisotropy, and large lateral variations in seismic wave velocities. Approaches such as these may be essential for unraveling the chemical, thermal, and dynamical state of this region.

Appendix A: Phases, Species, Components, and Parameters

[60] The simplified five-component system studied here (CaO-MgO-FeO-Al₂O₃-SiO₂) has the advantage that all phases that are expected to exist in the upper mantle are stable, and that the stability field of each of these phases is similar to that observed in natural peridotite compositions. The most abundant components that we have neglected (Na₂O, Cr₂O₃, NiO, MnO, and TiO₂) together make up approximately 2 wt % of typical peridotitic compositions [Irifune, 1994] and can be accommodated by our approach as experimental data on their effect on physical properties and phase equilibria continue to be gathered.

[61] We have assumed that the amount of CaO in orthopyroxene and C2/c, Al₂O₃ in clinopyroxene and C2/c, and the Ca-eskaloite component of clinopyroxene are negligible. We include also two transition zone phases (wadsleyite and ringwoodite) to better place our results in the context of seismic profiles that typically extend to depths greater than 400 km.

[62] Values of most parameters have either been directly measured or are constrained by experimental data (Table A1). Parameter values that have been estimated primarily on the basis of systematics (see below) are shown in italics. Values of V_0 , K_0 , K'_0 , and γ_0 for most species are taken from our previous compilations [Ita and Stixrude, 1992; Stixrude and Bukowinski, 1993]. Exceptions include those phases and species that were not included in our earlier studies (anorthite, spinel, Mg-tschermakite, Mg-diopside), for which the values were previously unknown (C2/c), or for which better determinations of some parameters are now available (e.g., forsterite and orthopyroxene K'_0 ; majorite V_0 , K_0 , K'_0 ; and grossular, K_0 , K'_0). New to this compilation are values of q_0 that we have constrained using measurements of the $P - V - T$ equation of state and/or measurements of the bulk modulus as a function of temperature. In the case of phases for which data on some species are absent or uncertain, we have assumed that K_0 , K'_0 , γ_0 , and q_0 are approximately constant across isostructural series. In a change of strategy from our earlier work, we have chosen to fit effective Debye temperatures to experimentally determined third law entropies at 1000 K where these are available. We have found that this procedure produces fits to heat capacity and enthalpy

data at high temperature that are nearly as good as our previous work while providing a much better description of the entropy. For those species for which the entropy is experimentally unconstrained or uncertain, we have followed the procedure of Akaogi *et al.* [1989] by estimating the entropy on the basis of Clapeyron slopes of phase transformations. Values of F_0 were determined by fitting to a large number of phase equilibrium data in the systems MS, MFS, MAS, CMAS, CFS, and CMS, as well as data on whole rock peridotite compositions.

[63] The entropy and volume of solution are assumed to be ideal. The entropy and enthalpy of mixing are computed via the sublattice model [Hillert and Staffansson, 1970]. We have approximated mixing in garnet-majorite by assuming two distinct octahedral sites and complete Mg-Si order over these sites. In spinel, we have approximated disorder in the end-members by assuming a fixed normal (inverse) component that approximates the experimentally observed temperature-dependent cation ordering over the temperature range that is most relevant to the low-velocity zone [Redfern *et al.*, 1999]. In orthopyroxene, we have assumed complete Mg-Fe-Al disorder on the octahedral sites and complete order on the tetrahedral sites [Wood and Holloway, 1984]. Excess enthalpy is included at the lowest order approximation (symmetric regular solution) for the following interactions with values of the Margules W parameter in kJ mol⁻¹ in parentheses: Ca-Mg on the larger octahedral site in clinopyroxene (26.3), and Mg-Fe interactions in olivine (7.2), wadsleyite (1.5), ringwoodite (3.9), and spinel (7.2). These values are determined by a combination of phase equilibrium, thermochemical and element partitioning data. The elastic moduli of solid solutions are computed as volume-weighted averages of the inverse moduli of the end-members [Ita and Stixrude, 1992].

[64] Values of the shear modulus are constrained by experimental measurements at ambient conditions. For those species for which no data exists we have estimated values based on $V_S - \rho$ systematics [Anderson *et al.*, 1968]. Values of G' and η_S are based on in situ high-pressure and/or high-temperature measurements. Where no data are available, we have either assumed that values are approximately constant across isostructural series or used systematic relations: for G'_0 we use the G'_0 versus G_0/K_0 systematic suggested by Duffy and Anderson [1989]; for η_{S0} , we have used a relationship between dG/dT versus G'_0 . The trends of these systematics are defined by the geophysically relevant species in our compilation.

[65] **Acknowledgments.** The authors thank Don Anderson, James Gaherty, Pierre Vacher, and two anonymous referees for their reviews of the manuscript, and Don Forsyth for a review of an earlier version. This work was partly supported by the CSEDI program of the National Science Foundation under grant EAR-0079980, and by fellowships from the David and Lucile Packard and the Alfred P. Sloan Foundations awarded to Lithgow-Bertelloni.

References

- Akaogi, M., E. Ito, and A. Navrotsky (1989), Olivine-modified spinel-spinel transitions in the system $\text{Mg}_2\text{SiO}_4\text{-Fe}_2\text{SiO}_4$: Calorimetric measurements, thermochemical calculation, and geophysical application, *J. Geophys. Res.*, **94**, 15,671–15,685.
- Akimoto, S., and Y. Syono (1970), High-pressure decomposition of the system $\text{FeSiO}_3\text{-MgSiO}_3$, *Phys. Earth Planet. Inter.*, **3**, 186–188.
- Anderson, D. L. (1989), *Theory of the Earth*, Blackwell Sci., Malden, Mass.
- Anderson, D. L., and J. D. Bass (1984), Mineralogy and composition of the upper mantle, *Geophys. Res. Lett.*, **11**, 637–640.
- Anderson, D. L., and C. Sammis (1969), The low velocity zone, *Geophys. Int.*, **9**, 3–19.
- Anderson, O. L., and D. G. Isaak (1995), Elastic constants of mantle minerals at high temperature, in *Mineral Physics and Crystallography: A Handbook of Physical Constants, Ref. Shelf*, vol. 2, edited by T. J. Ahrens, pp. 64–97, AGU, Washington, D. C.
- Anderson, O. L., E. Schreiber, and R. C. Lieberman (1968), Some elastic constant data on minerals relevant to geophysics, *Rev. Geophys.*, **6**, 491–524.
- Angel, R. J. (1988), High-pressure structure of anorthite, *Am. Mineral.*, **73**, 1114–1119.
- Angel, R. J., A. Chopelas, and N. L. Ross (1992), Stability of high-density clinostate at upper-mantle pressures, *Nature*, **358**, 322–324.
- Anovitz, L. M., E. J. Essene, G. W. Metz, S. R. Bohlen, E. F. Westrum, and B. S. Hemingway (1993), Heat-capacity and phase-equilibria of almandine, $\text{Fe}_3\text{Al}_2\text{Si}_3\text{O}_{12}$, *Geochim. Cosmochim. Acta*, **57**, 4191–4204.
- Bass, J. D. (1995), Elasticity of minerals, glasses, and melts, in *Mineral Physics and Crystallography: A Handbook of Physical Constants, Ref. Shelf*, vol. 2, edited by T. J. Ahrens, pp. 45–63, AGU, Washington, D. C.
- Berman, R. G. (1988), Internally-consistent thermodynamic data for minerals in the system $\text{Na}_2\text{O-K}_2\text{O-CaO-MgO-FeO-Fe}_2\text{O}_3\text{-Al}_2\text{O}_3\text{-SiO}_2\text{-TiO}_2\text{-H}_2\text{O-CO}_2$, *J. Petrol.*, **29**, 445–522.
- Birch, F. (1969), Density and composition of the upper mantle: First approximation as an olivine layer, in *The Earth's Crust and Upper Mantle: Structure, Dynamic Processes, and Their Relation to Deep-Seated Geological Phenomena*, *Geophys. Monogr. Ser.*, vol. 13, edited by P. J. Hart, pp. 18–36, AGU, Washington, D. C.
- Bunge, H. P., Y. Ricard, and J. Matas (2001), Non-adiabaticity in mantle convection, *Geophys. Res. Lett.*, **28**, 879–882.
- Cammarano, F., S. Goes, P. Vacher, and D. Giardini (2003), Inferring upper-mantle temperatures from seismic velocities, *Phys. Earth Planet. Inter.*, **138**, 197–222.
- Chai, M., J. M. Brown, and L. J. Slutsky (1997), The elastic constants of an aluminous orthopyroxene to 12.5 GPa, *J. Geophys. Res.*, **102**, 14,779–14,785.
- Christensen, U. (1995), Effects of phase transitions on mantle convection, *Annu. Rev. Earth Planet. Sci.*, **23**, 65–87.
- Conrad, P. G., C. S. Zha, H. K. Mao, and R. J. Hemley (1999), The high-pressure, single-crystal elasticity of pyrope, grossular, and andradite, *Am. Mineral.*, **84**, 374–383.
- Davies, G. F. (1974), Effective elastic-moduli under hydrostatic stress: 1. Quasi-harmonic theory, *J. Phys. Chem. Solids*, **35**, 1513–1520.
- Davies, G. F., and A. M. Dziewonski (1975), Homogeneity and constitution of Earth's lower mantle and outer core, *Phys. Earth Planet. Inter.*, **10**, 336–343.
- Downs, J. W., and M. S. T. Bukowski (1997), Variationally induced breathing equations of state of pyrope, grossular, and majorite garnets, *Geophys. Res. Lett.*, **24**, 1959–1962.
- Duffy, T. S., and D. L. Anderson (1989), Seismic velocities in mantle minerals and the mineralogy of the upper mantle, *J. Geophys. Res.*, **94**, 1895–1912.
- Dziewonski, A. M., and D. L. Anderson (1981), Preliminary reference Earth model, *Phys. Earth Planet. Inter.*, **25**, 297–356.
- Fei, Y. (1995), Thermal expansion, in *Mineral Physics and Crystallography: A Handbook of Physical Constants, Ref. Shelf*, vol. 2, edited by T. J. Ahrens, pp. 29–44, AGU, Washington, D. C.
- Fei, Y. W., and S. K. Saxena (1990), Internally consistent thermodynamic data and equilibrium phase-relations for compounds in the system MgO-SiO_2 at high-pressure and high-temperature and high-temperature, *J. Geophys. Res.*, **95**, 6915–6928.
- Fei, Y., H. K. Mao, and B. O. Mysen (1991), Experimental-determination of element partitioning and calculation of phase-relations in the MgO-FeO-SiO_2 system at high-pressure and high-temperature, *J. Geophys. Res.*, **96**, 2157–2169.
- Fei, Y., H. Mao, J. Shu, G. Parthasarathy, W. A. Bassett, and J. Ko (1992), Simultaneous high-P, high-T X-ray diffraction study of $\beta\text{-(Mg, Fe)}_2\text{SiO}_4$ to 26 GPa and 900 K, *J. Geophys. Res.*, **97**, 4489–4495.
- Flesch, L. M., B. S. Li, and R. C. Liebermann (1998), Sound velocities of polycrystalline MgSiO_3 -orthopyroxene to 10 GPa at room temperature, *Am. Mineral.*, **83**, 444–450.
- Gaherty, J. B., and T. H. Jordan (1995), Lehmann discontinuity as the base of an anisotropic layer beneath continents, *Science*, **268**, 1468–1471.
- Gaherty, J. B., M. Kato, and T. H. Jordan (1999a), Seismological structure of the upper mantle: A regional comparison of seismic layering, *Phys. Earth Planet. Inter.*, **110**, 21–41.

- Gaherty, J. B., Y. B. Wang, T. H. Jordan, and D. J. Weidner (1999b), Testing plausible upper-mantle compositions using fine-scale models of the 410-km discontinuity, *Geophys. Res. Lett.*, **26**, 1641–1644.
- Gasparik, T. (1990), Phase-relations in the transition zone, *J. Geophys. Res.*, **95**, 15,751–15,769.
- Ghiorso, M. S., and R. O. Sack (1995), Chemical mass-transfer in magmatic processes: 4. A revised and internally consistent thermodynamic model for the interpolation and extrapolation of liquid-solid equilibria in magmatic systems at elevated-temperatures and pressures, *Contrib. Mineral. Petrol.*, **119**, 197–212.
- Graham, E. K., J. A. Schwab, S. M. Sopkin, and H. Takei (1988), The pressure and temperature-dependence of the elastic properties of single-crystal fayalite Fe_2SiO_4 , *Phys. Chem. Miner.*, **16**, 186–198.
- Grand, S. P., and D. V. Helmberger (1984), Upper mantle shear structure of North-America, *Geophys. J. R. Astron. Soc.*, **76**, 399–438.
- Graves, R. W., and D. V. Helmberger (1988), Upper mantle cross-section from Tonga to Newfoundland, *J. Geophys. Res.*, **93**, 4701–4711.
- Green, D. H., and T. J. Falloon (1998), Pyrolite: A ringwood concept and its current expression, in *The Earth's Mantle*, edited by I. Jackson, pp. 311–378, Cambridge Univ. Press, New York.
- Green, D. H., and R. C. Liebermann (1976), Phase-equilibria and elastic properties of a pyrolite model for oceanic upper mantle, *Tectonophysics*, **32**, 61–92.
- Gu, Y. J., A. M. Dziewonski, and G. Ekstrom (2001), Preferential detection of the Lehmann discontinuity beneath continents, *Geophys. Res. Lett.*, **28**, 4655–4658.
- Gung, Y. C., M. Panning, and B. Romanowicz (2003), Global anisotropy and the thickness of continents, *Nature*, **422**, 707–711.
- Gutenberg, B. (1959), *Physics of the Earth's Interior*, Springer, New York.
- Hacker, B. R., G. A. Abers, and S. M. Peacock (2003), Subduction factory: 1. Theoretical mineralogy, densities, seismic wave speeds, and H_2O contents, *J. Geophys. Res.*, **108**(B1), 2029, doi:10.1029/2001JB001127.
- Hales, A. L. (1969), A seismic discontinuity in lithosphere, *Earth Planet. Sci. Lett.*, **7**, 44–46.
- Hammond, W. C., and E. D. Humphreys (2000), Upper mantle seismic wave velocity: Effects of realistic partial melt geometries, *J. Geophys. Res.*, **105**, 10,975–10,986.
- Harvie, C. E., J. P. Greenberg, and J. H. Weare (1987), A chemical-equilibrium algorithm for highly nonideal multiphase systems: Free-energy minimization, *Geochim. Cosmochim. Acta*, **51**, 1045–1057.
- Haselton, H. T., R. A. Robie, and B. S. Hemingway (1987), Heat-capacities of synthetic hedenbergite, ferrobustamite, and $\text{CaFeSi}_2\text{O}_6$ glass, *Geochim. Cosmochim. Acta*, **51**, 2211–2217.
- Hillert, M., and L. I. Staffansson (1970), Regular solution model for stoichiometric phases and ionic melts, *Acta Chem. Scand.*, **24**, 3618–3626.
- Hirschmann, M. M., and E. M. Stolper (1996), A possible role for garnet pyroxenite in the origin of the “garnet signature” in MORB, *Contrib. Mineral. Petrol.*, **124**, 185–208.
- Hirschmann, M. M., T. Kogiso, M. B. Baker, and E. M. Stolper (2003), Alkaline magmas generated by partial melting of garnet pyroxenite, *Geology*, **31**, 481–484.
- Hirth, G., and D. L. Kohlstedt (1996), Water in the oceanic upper mantle: Implications for rheology, melt extraction and the evolution of the lithosphere, *Earth Planet. Sci. Lett.*, **144**, 93–108.
- Holland, T. J. B., and R. Powell (1990), An enlarged and updated internally consistent thermodynamic dataset with uncertainties and correlations: The system $\text{K}_2\text{O}-\text{Na}_2\text{O}-\text{CaO}-\text{MgO}-\text{MnO}-\text{FeO}-\text{Fe}_2\text{O}_3-\text{Al}_2\text{O}_3-\text{TiO}_2-\text{SiO}_2-\text{C}-\text{H}_2\text{O}_2$, *J. Metamorph. Geol.*, **8**, 89–124.
- Hugh-Jones, D. A., and R. J. Angel (1997), Effect of Ca^{2+} and Fe^{2+} on the equation of state of MgSiO_3 orthopyroxene, *J. Geophys. Res.*, **102**, 12,333–12,340.
- Hugh-Jones, D. A., A. B. Woodland, and R. J. Angel (1994), The structure of high-pressure C_2/c ferrosilite and crystal-chemistry of high-pressure C_2/c pyroxenes, *Am. Mineral.*, **79**, 1032–1041.
- Irfune, T. (1993), Phase transformations in the Earth's mantle and subducting slabs: Implications for their compositions, seismic velocity and density structures and dynamics, *Island Arc*, **2**, 55–71.
- Irfune, T. (1994), Absence of an aluminous phase in the upper part of the Earth's lower mantle, *Nature*, **370**, 131–133.
- Irfune, T., and M. Isshiki (1998), Iron partitioning in a pyrolite mantle and the nature of the 410-km seismic discontinuity, *Nature*, **392**, 702–705.
- Irfune, T., and A. E. Ringwood (1987), Phase-transformations in a harzburgite composition to 26 GPa: Implications for dynamical behavior of the subducting slab, *Earth Planet. Sci. Lett.*, **86**, 365–376.
- Ita, J., and L. Stixrude (1992), Petrology, elasticity, and composition of the mantle transition zone, *J. Geophys. Res.*, **97**, 6849–6866.
- Ito, E., and E. Takahashi (1989), Postspinel transformations in the system $\text{Mg}_2\text{SiO}_4\text{-Fe}_2\text{SiO}_4$ and some geophysical implications, *J. Geophys. Res.*, **94**, 10,637–10,646.
- Jackson, I., J. D. Fitz Gerald, U. H. Faul, and B. H. Tan (2002), Grain-size-sensitive seismic wave attenuation in polycrystalline olivine, *J. Geophys. Res.*, **107**(B12), 2360, doi:10.1029/2001JB001225.
- Jackson, I., U. H. Faul, J. D. Fitz Gerald, and B. H. Tan (2004), Shear wave attenuation and dispersion in melt-bearing olivine polycrystals: 1. Specimen fabrication and mechanical testing, *J. Geophys. Res.*, **109**, B06201, doi:10.1029/2003JB002406.
- Jackson, J. M., S. V. Sinogeikin, and J. D. Bass (1999), Elasticity of MgSiO_3 orthoenstatite, *Am. Mineral.*, **84**, 677–680.
- Jackson, J. M., S. V. Sinogeikin, and J. D. Bass (2000), Sound velocities and elastic properties of gamma- Mg_2SiO_4 to 873 K by Brillouin spectroscopy, *Am. Mineral.*, **85**, 296–303.
- Jamieson, H. E., and P. L. Roeder (1984), The distribution of Mg and Fe^{2+} between olivine and spinel at 1300°C, *Am. Mineral.*, **69**, 283–291.
- Jaupart, C., and J. C. Mareschal (1999), The thermal structure and thickness of continental roots, *Lithos*, **48**, 93–114.
- Jeanloz, R., and S. Morris (1987), Is the mantle geotherm subadiabatic, *Geophys. Res. Lett.*, **14**, 335–338.
- Jeanloz, R., and F. M. Richter (1979), Convection, composition, and the thermal state of the lower mantle, *J. Geophys. Res.*, **84**, 5497–5504.
- Karato, S., and H. Jung (1998), Water, partial melting and the origin of the seismic low velocity and high attenuation zone in the upper mantle, *Earth Planet. Sci. Lett.*, **157**, 193–207.
- Katsura, T., and E. Ito (1989), The system $\text{Mg}_2\text{SiO}_4\text{-Fe}_2\text{SiO}_4$ at high-pressures and temperatures - precise determination of stabilities of olivine, modified spinel, and spinel, *J. Geophys. Res.*, **94**, 15,663–15,670.
- Kennett, B. L. N. (1991), Seismic velocity gradients in the upper mantle, *Geophys. Res. Lett.*, **18**, 1115–1118.
- Kim, Y. H., L. C. Ming, M. H. Manghnani, and J. Ko (1991), Phase-transformation studies on a synthetic hedenbergite up to 26 GPa at 1200°C, *Phys. Chem. Miner.*, **17**, 540–544.
- Kinzler, R. J. (1997), Melting of mantle peridotite at pressures approaching the spinel to garnet transition: Application to mid-ocean ridge basalt petrogenesis, *J. Geophys. Res.*, **102**, 853–874.
- Klein, E. M., and C. H. Langmuir (1987), Global correlations of ocean ridge basalt chemistry with axial depth and crustal thickness, *J. Geophys. Res.*, **92**, 8089–8115.
- Knittle, E. (1995), Static compression measurements of equations of state, in *Mineral Physics and Crystallography: A Handbook of Physical Constants, Ref. Shelf*, vol. 2, edited by T. J. Ahrens, pp. 98–142, AGU, Washington, D. C.
- Krupka, K. M., R. A. Robie, B. S. Hemingway, D. M. Kerrick, and J. Ito (1985), Low-temperature heat-capacities and derived thermodynamic properties of anthophyllite, diopside, enstatite, bronzite, and wollastonite, *Am. Mineral.*, **70**, 249–260.
- Kumazawa, M., and O. L. Anderson (1969), Elastic moduli, pressure derivatives, and temperature derivatives of single-crystal olivine and single-crystal forsterite, *J. Geophys. Res.*, **74**, 5961–5972.
- Lambert, I. B., and P. J. Wyllie (1968), Stability of hornblende and a model for low velocity zone, *Nature*, **219**, 1240–1241.
- Lee, C. A. (2003), Compositional variation of density and seismic velocities in natural peridotites at STP conditions: Implications for seismic imaging of compositional heterogeneities in the upper mantle, *J. Geophys. Res.*, **108**(B9), 2441, doi:10.1029/2003JB002413.
- Levin, V., and J. Park (2000), Shear zones in the proterozoic lithosphere of the Arabian shield and the nature of the Hales discontinuity, *Tectonophysics*, **323**, 131–148.
- Li, B. S., and R. C. Liebermann (2000), Sound velocities of wadsleyite $\beta\text{-(Mg}_{0.88}\text{Fe}_{0.12})_2\text{SiO}_4$ to 10 GPa, *Am. Mineral.*, **85**, 292–295.
- Li, B. S., R. C. Liebermann, and D. J. Weidner (2001), P-V-Vp-Vs-T measurements on wadsleyite to 7 GPa and 873 K: Implications for the 410-km seismic discontinuity, *J. Geophys. Res.*, **106**, 30,579–30,591.
- McKenzie, D., and M. J. Bickle (1988), The volume and composition of melt generated by extension of the lithosphere, *J. Petrol.*, **29**, 625–679.
- Meng, Y., D. J. Weidner, G. D. Gwanmesia, R. C. Liebermann, M. T. Vaughan, Y. Wang, K. Leinenweber, R. E. Pacalo, A. Yeganeh-Haeri, and Y. Zhao (1993), In situ high P-T X ray diffraction studies on three polymorphs (α , β , γ) of Mg_2SiO_4 , *J. Geophys. Res.*, **98**, 22,199–22,208.
- Morishima, H., T. Kato, M. Suto, E. Ohtani, S. Urakawa, W. Utsumi, O. Shimomura, and T. Kikegawa (1994), The phase-boundary between $\alpha\text{-Mg}_2\text{SiO}_4$ and $\beta\text{-Mg}_2\text{SiO}_4$ determined by in-situ X-ray observation, *Science*, **265**, 1202–1203.
- Mueller, H. J., J. Lauterjung, F. R. Schilling, C. Lathe, and G. Nover (2002), Symmetric and asymmetric interferometric method for ultrasonic compressional and shear wave velocity measurements in piston-cylinder and multi-anvil high-pressure apparatus, *Eur. J. Mineral.*, **14**, 581–589.
- Nataf, H. C., I. Nakanishi, and D. L. Anderson (1986), Measurements of mantle wave velocities and inversion for lateral heterogeneities and anisotropy: 3. Inversion, *J. Geophys. Res.*, **91**, 7261–7307.

- Nickel, K. G. (1986), Phase-equilibria in the system $\text{SiO}_2\text{-MgO-Al}_2\text{O}_3\text{-CaO-Cr}_2\text{O}_3$ (SMACCR) and their bearing on spinel garnet ilmenite relationships, *Neues Jahrb. Mineral. Abh.*, 155, 259–287.
- Nishimura, C. E., and D. W. Forsyth (1989), The anisotropic structure of the upper mantle in the Pacific, *Geophys. J.*, 96, 203–229.
- Pacalo, R. E. G., and T. Gasparik (1990), Reversals of the orthoenstatite-clinoenstatite transition at high-pressures and high-temperatures, *J. Geophys. Res.*, 95, 15,853–15,858.
- Pacalo, R. E. G., and D. J. Weidner (1997), Elasticity of majorite, MgSiO_3 tetragonal garnet, *Phys. Earth Planet. Inter.*, 99, 145–154.
- Plank, T., and C. H. Langmuir (1992), Effects of the melting regime on the composition of the oceanic crust, *J. Geophys. Res.*, 97, 19,749–19,770.
- Press, W. H., S. A. Teukolsky, W. T. Vetterling, and B. P. Flannery (1992), *Numerical Recipes in FORTRAN: The Art of Scientific Computing*, Cambridge Univ. Press, New York.
- Redfern, S. A. T., R. J. Harrison, H. S. C. O'Neill, and D. R. R. Wood (1999), Thermodynamics and kinetics of cation ordering in MgAl_2O_4 spinel up to 1600°C from in situ neutron diffraction, *Am. Mineral.*, 84, 299–310.
- Revenaugh, J., and T. H. Jordan (1991), Mantle layering from ScS reverberations: 3. The upper mantle, *J. Geophys. Res.*, 96, 19,781–19,810.
- Richards, M. A., W. Yang, J. R. Baumgardner, and H. Bunge (2001), Role of a low-viscosity zone in stabilizing plate tectonics: Implications for comparative terrestrial planetology, *Geochim. Geophys. Geosyst.*, 2(8), doi:10.1029/2000GC000115.
- Ringwood, A. E. (1969), Composition and evolution of the upper mantle, in *The Earth's Crust and Upper Mantle: Structure, Dynamic Processes, and Their Relation to Deep-Seated Geological Phenomena*, *Geophys. Monogr. Ser.*, vol. 13, edited by P. J. Hart, pp. 1–17, AGU, Washington, D. C.
- Ringwood, A. E. (1979), *Origin of the Earth and Moon*, Springer, New York.
- Robie, R. A., B. S. Hemingway, and J. R. Fisher (1978), Thermodynamic properties of minerals and related substances at 298.15 K and 1 bar (105 pascals) pressure and at higher temperatures, *U.S. Geol. Surv. Bull.*, 1452.
- Robie, R. A., B. S. Hemingway, and H. Takei (1982), Heat-capacities and entropies of Mg_2SiO_4 , Mn_2SiO_4 , and Co_2SiO_4 between 5-K and 380-K, *Am. Mineral.*, 67, 470–482.
- Robinson, J. A. C., and B. J. Wood (1998), The depth of the spinel to garnet transition at the peridotite solidus, *Earth Planet. Sci. Lett.*, 164, 277–284.
- Romanowicz, B. (1995), A global tomographic model of shear attenuation in the upper mantle, *J. Geophys. Res.*, 100, 12,375–12,394.
- Romanowicz, B. (1998), Attenuation tomography of the Earth's mantle: A review of current status, *Pure Appl. Geophys.*, 153, 257–272.
- Romanowicz, B., and J. J. Durek (2000), Seismological constraints on attenuation in the Earth: A review, in *Earth's Deep Interior: Mineral Physics and Tomography from the Atomic to the Global Scale*, *Geophys. Monogr. Ser.*, vol. 117, edited by S. Karato et al., pp. 161–179, AGU, Washington, D. C.
- Sammis, C., D. Anderson, and T. Jordan (1970), Application of isotropic finite strain theory to ultrasonic and seismological data, *J. Geophys. Res.*, 75, 4478–4480.
- Sato, H., I. S. Sacks, and T. Murase (1989), The use of laboratory velocity data for estimating temperature and partial melt fraction in the low-velocity zone: Comparison with heat flow and electrical conductivity studies, *J. Geophys. Res.*, 94, 5689–5704.
- Schubert, G., C. Froidevaux, and D. A. Yuen (1976), Oceanic lithosphere and asthenosphere: Thermal and mechanical structure, *J. Geophys. Res.*, 81, 3525–3540.
- Shankland, T. J., and H. S. Waff (1977), Partial melting and electrical conductivity anomalies in upper mantle, *J. Geophys. Res.*, 82, 5409–5417.
- Sinogeikin, S. V., and J. D. Bass (2000), Single-crystal elasticity of pyrope and MgO to 20 GPa by Brillouin scattering in the diamond cell, *Phys. Earth Planet. Inter.*, 120, 43–62.
- Sinogeikin, S. V., and J. D. Bass (2002), Elasticity of Majorite and a Majorite-Pyrope solid solution to high pressure: Implications for the Transition Zone, *Geophys. Res. Lett.*, 29(2), 1017, doi:10.1029/2001GL013937.
- Sinogeikin, S. V., T. Katsura, and J. D. Bass (1998), Sound velocities and elastic properties of Fe-bearing wadsleyite and ringwoodite, *J. Geophys. Res.*, 103, 20,819–20,825.
- Sinogeikin, S. V., J. D. Bass, and T. Katsura (2001), Single-crystal elasticity of $\gamma\text{-(Mg}_{0.91}\text{Fe}_{0.09})_2\text{SiO}_4$ to high pressures and to high temperatures, *Geophys. Res. Lett.*, 28, 4335–4338.
- Skinner, B. J., and F. R. Boyd (1964), Aluminous enstatites, *Year Book Carnegie Inst. Washington*, 63, 163–165.
- Smyth, J. R., and T. C. McCormick (1995), Crystallographic data for minerals, in *Mineral Physics and Crystallography: A Handbook of Physical Constants, Ref. Shelf*, vol. 2, edited by T. J. Ahrens, pp. 1–17, AGU, Washington, D. C.
- Sobolev, S. V., and A. Y. Babeyko (1994), Modeling of mineralogical composition, density and elastic-wave velocities in anhydrous magmatic rocks, *Surv. Geophys.*, 15, 515–544.
- Stixrude, L., and M. S. T. Bukowski (1990), Fundamental thermodynamic relations and silicate melting with implications for the constitution of D'' , *J. Geophys. Res.*, 95, 19,311–19,325.
- Stixrude, L., and M. S. T. Bukowski (1993), Thermodynamic analysis of the system MgO-FeO-SiO_2 at high pressure and the structure of the lowermost mantle, in *Evolution of the Earth and Planets, Geophys. Monogr. Ser.*, vol. 74, edited by E. Takahashi, R. Jeanloz, and D. Rubie, pp. 131–142, AGU, Washington, D. C.
- Stixrude, L., and C. Lithgow-Bertelloni (2005), Thermodynamics of mantle minerals: 1. Physical properties, *Geophys. J. Int.*, in press.
- Su, W. J., R. L. Woodward, and A. M. Dziewonski (1994), Degree-12 model of shear velocity heterogeneity in the mantle, *J. Geophys. Res.*, 99, 6945–6980.
- Suzuki, A., E. Ohtani, H. Morishima, T. Kubo, Y. Kanbe, T. Kondo, T. Okada, H. Terasaki, T. Kato, and T. Kikegawa (2000), In situ determination of the phase boundary between wadsleyite and ringwoodite in Mg_2SiO_4 , *Geophys. Res. Lett.*, 27, 803–806.
- Taylor, W. R., and D. H. Green (1988), Measurement of reduced peridotite-C-O-H solidus and implications for redox melting of the mantle, *Nature*, 332, 349–352.
- Tequi, C., R. A. Robie, B. S. Hemingway, D. R. Neuville, and P. Richet (1991), Melting and thermodynamic properties of pyrope ($\text{Mg}_3\text{Al}_2\text{Si}_3\text{O}_{12}$), *Geochim. Cosmochim. Acta*, 55, 1005–1010.
- Thieblot, L., C. Tequi, and P. Richet (1999), High-temperature heat capacity of grossular ($\text{Ca}_3\text{Al}_2\text{Si}_3\text{O}_{12}$), enstatite (MgSiO_3), and titanite (CaTiSiO_5), *Am. Mineral.*, 84, 848–855.
- Tribaudino, M., M. Prencepio, F. Nestola, and M. Hanfland (2001), A P_{21}/c - C_2/c high-pressure phase transition in $\text{Ca}_{0.5}\text{Mg}_{1.5}\text{Si}_2\text{O}_6$ clinopyroxene, *Am. Mineral.*, 86, 807–813.
- Vacher, P., A. Mocquet, and C. Sotin (1998), Computation of seismic profiles from mineral physics: The importance of the non-olivine components for explaining the 660 km discontinuity, *Phys. Earth Planet. Inter.*, 106, 275–298.
- Verhoogen, J. (1965), Physics of convection currents in Earth's mantle: 22. Phase changes and convection in Earth's mantle, *Philos. Trans. R. Soc. London, Ser. A*, 258, 276–283.
- Wang, Y. B., D. J. Weidner, J. Z. Zhang, G. D. Gwanmesia, and R. C. Liebermann (1998), Thermal equation of state of garnets along the pyrope-majorite join, *Phys. Earth Planet. Inter.*, 105, 59–71.
- Wang, Z. C., and S. C. Ji (2001), Elasticity of six polycrystalline silicate garnets at pressure up to 3.0 GPa, *Am. Mineral.*, 86, 1209–1218.
- Watt, J. P., G. F. Davies, and R. J. O. Connell (1976), The elastic properties of composite materials, *Rev. Geophys.*, 14, 541–563.
- Webb, S. C., and D. W. Forsyth (1998), Structure of the upper mantle under the EPR from waveform inversion of regional events, *Science*, 280, 1227–1229.
- Weidner, D. J. (1985), A mineral physics test of a pyrolite mantle, *Geophys. Res. Lett.*, 12, 417–420.
- Wood, B. J., and J. R. Holloway (1984), A thermodynamic model for subsolidus equilibria in the system $\text{CaO-MgO-Al}_2\text{O}_3\text{-SiO}_2$, *Geochim. Cosmochim. Acta*, 48, 159–176.
- Wood, B. J., and D. A. Yuen (1983), The role of lithospheric phase-transitions on seafloor flattening at old ages, *Earth Planet. Sci. Lett.*, 66, 303–314.
- Woodland, A. B. (1998), The orthorhombic to high-p monoclinic phase transition in Mg-Fe pyroxenes: Can it produce a seismic discontinuity?, *Geophys. Res. Lett.*, 25, 1241–1244.
- Yoneda, A. (1990), Pressure derivatives of elastic-constants of single-crystal MgO and MgAl_2O_4 , *J. Phys. Earth*, 38, 19–55.
- Zha, C. S., T. S. Duffy, R. T. Downs, H. K. Mao, and R. J. Hemley (1996), Sound velocity and elasticity of single-crystal forsterite to 16 GPa, *J. Geophys. Res.*, 101, 17,535–17,545.
- Zhang, J. Z., and C. Herzberg (1994), Melting experiments on anhydrous peridotite KLB-1 from 5.0 to 22.5 GPa, *J. Geophys. Res.*, 99, 17,729–17,742.
- Zhao, L. S., and D. V. Helmberger (1993), Upper-mantle compressional velocity structure beneath the northwest Atlantic Ocean, *J. Geophys. Res.*, 98, 14,185–14,196.
- Zhao, Y., R. B. V. Dreele, J. Zhang, and D. J. Weidner (1998), Thermoelastic equation of state of monoclinic pyroxene: $\text{CaMgSi}_2\text{O}_6$, *Rev. High Pressure Sci. Technol.*, 7, 25–27.
- Zhao, Y. S., D. Schiferl, and T. J. Shankland (1995), A high P-T single-crystal X-ray diffraction study of thermoelasticity of MgSiO_3 orthoenstatite, *Phys. Chem. Miner.*, 22, 393–398.

C. Lithgow-Bertelloni and L. Stixrude, Department of Geological Sciences, University of Michigan, 425 E. University Ave., Ann Arbor, MI 48109-1063, USA. (stixrude@umich.edu)